# 2D boron nitride synthesis via electromagnetic induction heating: Experiments and thermochemical modeling

Wafa Alimi, Ivaylo Hinkov, Christophe Arnold, Julien Barjon, Salim Mourad Chérif, Samir Farhat

# 2D Boron Nitride Synthesis *via* Electromagnetic Induction Heating: Experiments and Thermochemical Modeling

**Wafa Alimi[1], Ivaylo Hinkov[2], Christophe Arnold[3], Julien Barjon[3], Salim Mourad Chérif[1], and Samir Farhat[1,*]**

[1] Université Sorbonne Paris Nord, Laboratoire des Sciences des Procédés et des Matériaux, CNRS, LSPM-UPR 3407, F-93430, Villetaneuse, France
[2] Department of Chemical Engineering, University of Chemical Technology and Metallurgy, 8 Boulevard St. Kliment Ohridski, 1756 Sofia, Bulgaria
[3] GEMaC, UVSQ, CNRS, Université Paris Saclay, France

**Abstract :**

We present a novel approach for synthesizing few-layered two-dimensional boron nitride (FL-BN) using low pressure chemical vapor deposition (LPCVD). In our approach, a radio frequency (RF) magnetic field was generated to inductively heat copper foils. The process involved placing the copper foil on a tungsten substrate and applying inductive heating until the copper melted within about two minutes. Subsequently, boron-nitrogen precursors were generated *via* the decomposition of ammonia borane at approximately 80°C, and these species were then transported by an argon/hydrogen flow to the liquid Cu, promoting the nucleation and growth of h-BN. Thermochemical calculations performed by using ChemkinPro software indicated the prevalence of B-N-H species within the temperature range of 20°C to 1100°C, surpassing the melting point of copper. The resulting h-BN layers exhibited exceptional structural integrity, as confirmed by Raman and X-ray photoelectron spectroscopy (XPS) analyses. Furthermore, room-temperature cathodoluminescence (CL) measurements revealed a prominent excitonic peak at the photon energy position 5.77 eV (215 nm), which is a consequence of the deep UV optical gap of the h-BN crystal. Thus, the inductive heating process demonstrates significant potential for large-scale and rapid manufacturing of h-BN, offering enhanced energy efficiency. Additionally, we introduce a new conceptual design enabling precise control of the synthesis parameters, thus facilitating scalable production of high-quality h-BN films.

Keywords: Boron nitride - Copper - Inductive Heating – Ammonia Borane – Modeling

*corresponding author: farhat@lspm.cnrs.fr

## 1. Introduction

Two-dimensional (2D) few-layered boron nitride (FL-BN), also known as "white graphene," comprises alternating layers of $sp^2$-bonded boron and nitrogen atoms arranged in a hexagonal lattice. This material has been demonstrated to be an ideal complementary material for various other 2D materials as substrates and encapsulating layers. Unlike semi-metallic graphene, reducing the thickness of h-BN to the atomic level yields a notable optical phonon mode and wide direct band gap energy of approximately 5.9 eV [1]. Additionally, h-BN tends to absorb light in the ultraviolet (UV) range, remaining transparent in the visible spectrum, hence earning its "white graphene" moniker. The distinct vibrational signature of the optical phonon mode in h-BN arises from the specific arrangement of its boron and nitrogen atoms, significantly influencing its thermal and electronic properties. The wide band gap reduces available energy levels for phonon scattering, thereby promoting efficient heat transfer. Although graphene boasts high thermal conductivity (5300 W/mK at room temperature [2]), its electrical conductivity limits its direct use in numerous thermal dissipation applications, such as electronics. In contrast, monolayer h-BN exhibits a thermal conductivity of 751 W/mK at room temperature, ranking second among all semiconductors and insulators by weight [3]. The substantial band gap energy of h-BN enhances its mechanical stability and strength, reducing its susceptibility to chemical reactions and bolstering its chemical stability. Few-layered FL-BN crystals or monolayers have thus become crucial elements in van der Waals heterostructures, capitalizing on good thermal conductivity, mechanical flexibility, chemical stability, and low dielectric constant. Atomically thin h-BN finds applications in various fields, including single photon emitters, dielectrics in nanoelectronic devices, thin deep ultraviolet (DUV) light emitters for optoelectronics and detectors, and as a protective coating layer [4-6]. Moreover, h-BN's atomically smooth and ultra-flat surface, devoid of dangling bonds and trapped charges, makes it an ideal substrate for graphene, enhancing electron mobility by an order of magnitude compared to conventional silicon dioxide ($SiO_2$) substrates [7]. For achieving large-scale production of high-quality h-BN with homogeneous layers, bottom-up techniques such as wafer-scale chemical vapor deposition (CVD) are favored over physical vapor deposition (PVD) and molecular beam epitaxy (MBE) due to their cost-effectiveness [1].

While mechanical exfoliation from bulk h-BN crystals yields excellent-quality few-layer to monolayer h-BN, it is limited to micrometer sizes [8]. To overcome this limitation, bottom-up techniques enable the production of monolayer and multilayer h-BN films over large surfaces,

with wafer-scale CVD being a common choice to realize the full potential of ultrathin layered h-BN [1]. Chemical vapor deposition of hexagonal boron nitride can use diverse precursor sources, each contributing to h-BN formation through nucleation and growth processes on various substrates, including polycrystalline transition metal catalysts Cu [9], Ni [10], Pt [11], Fe [12], monocristals Cu(111) [13], Ni(111) [14], Pt(111) [15], metal alloys Cu-Ni [16] and ceramics such as sapphire ($Al_2O_3$) [17], silicon carbide (SiC) [18], and aluminum nitride (AlN) [19]. Some studies employ metal in liquid states, especially those with low melting points such as Cu [20-24] and Au [25].

The choice of precursor is contingent upon the synthesis method and the required properties of the resulting h-BN material. Indeed, meticulous selection and control of precursors are essential for achieving the appropriate purity, morphology, and characteristics of h-BN layers. Common boron and nitrogen precursor sources include cyclic boron-nitrogen borazine (BZ or $B_3N_3H_6$) [26-30] and ammonia borane (AB or $H_3NBH_3$) [31-34]. These precursors have the advantage of maintaining a one-to-one B/N ratio; however, their thermal decomposition prior to h-BN growth is not yet fully understood. Borazine typically remains in a liquid state at standard room temperature and pressure and exhibits stability at elevated temperatures. Nonetheless, it is highly sensitive to oxygen and moisture, leading to oxidation and hydrolysis reactions, respectively, thereby compromising its stability and potentially generating boron and nitrogen oxides, boric acid ($H_3BO_3$), and ammonia. This presents challenges in the storage and handling of borazine within controlled environments. Conversely, ammonia borane remains solid at room temperature and pressure, decomposing at temperatures below 110°C to yield various volatile boron-nitrogen compounds and solid polyaminoborane (PAB or $(NH_2BH_2)_n$). Due to the high polarity of the $H_3N$-$BH_3$ molecule, it exists in a crystalline solid state at room temperature, rather than in a gaseous form. Although ammonia borane has garnered scientific interest since its first synthesis in the 1950s as part of a US government research program focused on studying high-energy densities boron-based jet fuels, the decomposition of AB has been extensively studied. However, there has been limited research conducted to explore the reaction pathways detailing the polymerization and cyclization steps involved in forming polyaminoborane (PAB) and higher molecular weight species. These include ring-containing species that constitute the later stages of AB decomposition.

It is essential to design chemical vapor deposition reactors that can accurately regulate the domain size and morphology of h-BN to achieve optimal material properties. Therefore, it is necessary to control the nucleation and growth steps independently. However, these steps are

constrained by the thermodynamics and the gas phase kinetics in the reactor. The growth of h-BN is considered as thermally activated process since most chemical reactions are thermodynamically endothermic. Consequently, the essential aspect of the CVD method remains the thermal activation of the chemical system and control of the temperature gradient over the substrate during growth. Several CVD methods have been proposed to activate gas and surface reactions. These methods include thermal CVD (TCVD), as referenced in [1], and plasma-enhanced CVD (PECVD), as seen in [35-37], among others. In TCVD systems, heating is achieved using hot-wall ovens, whereas PECVD process employs cold-wall reactors in which inlet gases are ionized and dissociated through electron impact and active ions and radicals facilitate h-BN growth at lower temperatures. However, for large-scale h-BN growth, both TCVD and PECVD systems become less energy efficient due to the larger gas volume, which necessitates higher power for thermal activation. In this context, inductive heating (IH) presents a significant advantage over conventional thermal heating methods, as it utilizes radio frequency magnetic fields to inductively heat only the metal substrate through the Joule effect, regardless of the reactor volume. . This allows for exceptionally fast FL-BN synthesis, increasing the substrate temperature from room temperature to about 1100°C in only two minutes. Furthermore, inductive heating overcomes challenges associated with traditional TCVD methods, where heat is supplied by ovens, requiring a larger volume for scaling up to larger copper substrates. However, maintaining precise temperature control becomes increasingly arduous with larger heating zones. Inductive heating presents a contactless solution for heating in cold-wall CVD systems, specifically targeting the thin copper foil without heating the surrounding gas. This method enhances control and efficiency in FL-BN synthesis.

The CVD growth of h-BN is a complex and dynamic process involving several interrelated stages. Initially, boron and nitrogen species are generated and transported through the gas phase. This is followed by interactions on the catalyst surface, where various reactions take place. Subsequently, diffusion occurs either through the bulk of the catalyst or along its surface. Additionally, the capture and release of precursors on the catalyst are crucial steps in the process. Finally, nucleation and growth of the crystal take place, which encompasses the attachment and detachment of adatoms, as well as their movement across the surface. Despite conceptual similarities between the CVD of graphene and that of h-BN, differences exist. Indeed, unlike graphene growth, where carbon precursors nucleate with difficulty on the growing graphene providing clear separation between nucleation and growth stages, the

growth of monolayer hexagonal boron nitride is yet very challenging, especially if polycrystalline copper is used as a catalyst. Hence monolayer graphene domains can coalesce at the end of growth forming single-layer graphene. In contrast, during h-BN growth, nucleation leads to mono domains, which in turn are prone to secondary nucleation. Hence, separating nucleation and growth stages, as possible for graphene, seems more difficult for h-BN. For these reasons, it is essential to understand the mechanism of decomposition of ammonia borane and how vapor-phase precursors generated behave upon the first heating region down to the inductively heated copper substrate and which processes and precursors control the h-BN nucleation and growth.

In this study, we present, to the best of our knowledge, the first demonstration of uniformly distributed triangular FL-BN domains deposition by inductive heating process. This was achieved by utilizing ammonia borane as a precursor and performing LPCVD on a liquid copper substrate that was inductively heated. The resulting FL-BN films exhibited hierarchically organized patterns of high quality, as confirmed by scanning electron microscopy (SEM), X-ray photoelectron spectroscopy (XPS), and Raman spectroscopy analyses. Furthermore, cathodoluminescence (CL) spectroscopy was employed to acquire the ultraviolet emission spectrum of FL-BN. This involved irradiating an electron beam on the sample to excite the valence band electrons, thereby observing the light emission during electron-hole recombination. Additionally, potential precursors for h-BN growth in the B-N-H system will be explored through thermochemical modeling of ammonia borane decomposition using Chemkin software. This offers valuable insights into potential precursors for h-BN growth, enhancing our understanding of the underlying chemical processes involved. This approach not only aids in identifying promising candidates but also provides a framework for optimizing growth conditions, thereby advancing the development of h-BN-based materials and technologies.

## 2. Materials and Methods

### 2.1 Hexagonal boron nitride synthesis and transfer

The FL-BN synthesis was conducted through chemical vapor deposition using the inductive heating reactor depicted in figure 1(a). Specifically, our setup incorporates solid ammonia borane with independent heating control upstream of the induction coils, where FL-BN growth occurs on the heated liquid copper surface. To ensure a uniform electromagnetic field,

we employed circular coils in a Helmholtz configuration, as detailed in our previous publications on graphene synthesis [38,39].

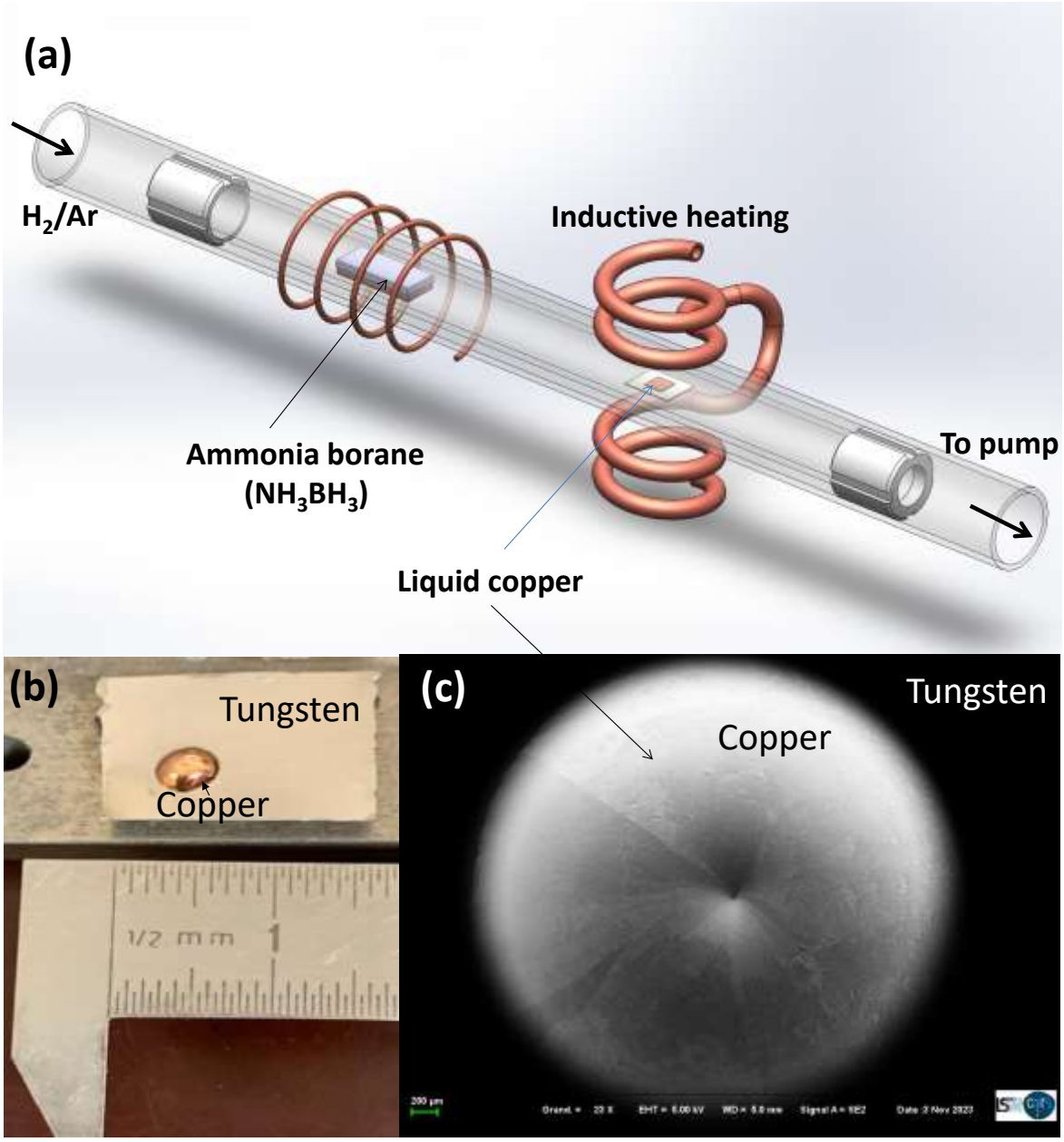


**Figure 1.** (a) Schematic of the inductive heating reactor setup. (b) Photography of the melted copper on tungsten. (c) SEM image of the solidified copper droplet after FL-BN deposition (scale bar 200 µm).

This setup includes a radio frequency power source (Easy HEAT Ambrell 2.5 KW) at 215 kHz, Helmholtz-like coils (3.62 cm diameter), a heat exchanger, and a pumping system with a turbo and backing pump. The Helmholtz coils are identical circular magnetic coils, each with two turns, carrying equal currents in the same direction. A copper foil atop a tungsten foil was

placed in a quartz tube (1.35 cm inner diameter) centered in the coils, with a supporting quartz tube (2.5 cm inner diameter) connected to gas inlets and the vacuum pump. Inductive heating, as shown in figure 1(b) and figure 1(c), completely melted the Cu foil, spreading it uniformly on the W substrate.

The temperature of the copper was measured using an optical pyrometer (Yokogawa), which has an optical resolution of 45:1, a thermal resolution of 0.1 °C, and a fast response time of 2 ms. Gas flow rates were regulated by Ar and $H_2$ flowmeters located at the reactor inlet. Ammonia borane (97% purity, Sigma-Aldrich) was positioned in a nickel boat located 16 cm away from Cu/W. When heated to (80±0.5) °C *via* an external heating system (Julabo LC4 – 2 kW), ammonia borane decomposed into various gaseous species along with solid polyaminoborane.

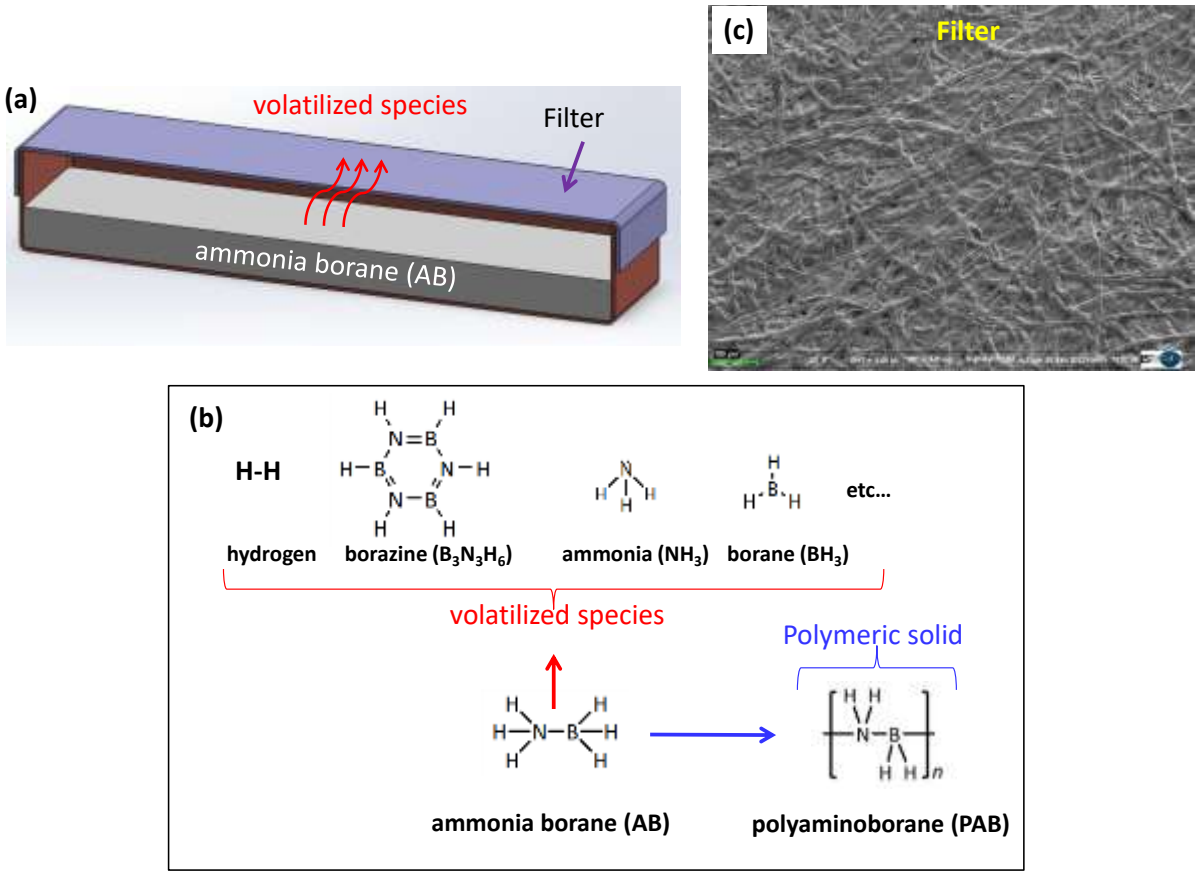


**Figure 2.** (a) Cross-section of the nickel receptacle containing AB and equipped with a nanometric filter with pore sizes of 50 nm. (b) Reaction scheme of the thermal decomposition of AB into volatile products and polymeric solid. (c-) SEM micrographs of the filter used to retain nanoparticles larger than 50 nm (scale bare 100 µm).

The temperature of the ammonia borane was measured using a thermocouple integrated into the heating system with a PID controller and a thermal resolution of 0.1 °C. A typical temperature profile with a heating rate of 8°C/min is given in figure S1 of the supplementary materials. A reaction scheme depicting the decomposition of AB is provided in figure 2(a) and figure 2(b). Subsequently, several nitrogen- and boron-containing species are volatilized alongside $H_2$ and nanoparticles. These volatilized B and N species act precursors for h-BN growth, whereas nanoparticles are undesirable as they may contaminate and disturb the growing h-BN. The formation of these nanoparticles is amplified by the foaming, where ammonia borane expands during heating, potentially producing small polymeric nanoparticles carried by the flowing $Ar/H_2$ gases to the copper surface. To safeguard against contamination of the growing h-BN with these nanoparticles, a filter with a pore size of approximately 50 nm (figure 2(c)) was installed on the nickel boat. The system can then be decomposed into two heating regions: region A for heating the ammonia borane powder with independent heating control, and region B for inductively heating the metal substrate controlled by the current imposed to the coils. Figure 3 depicts the standard procedure for inductive heating CVD h-BN synthesis.

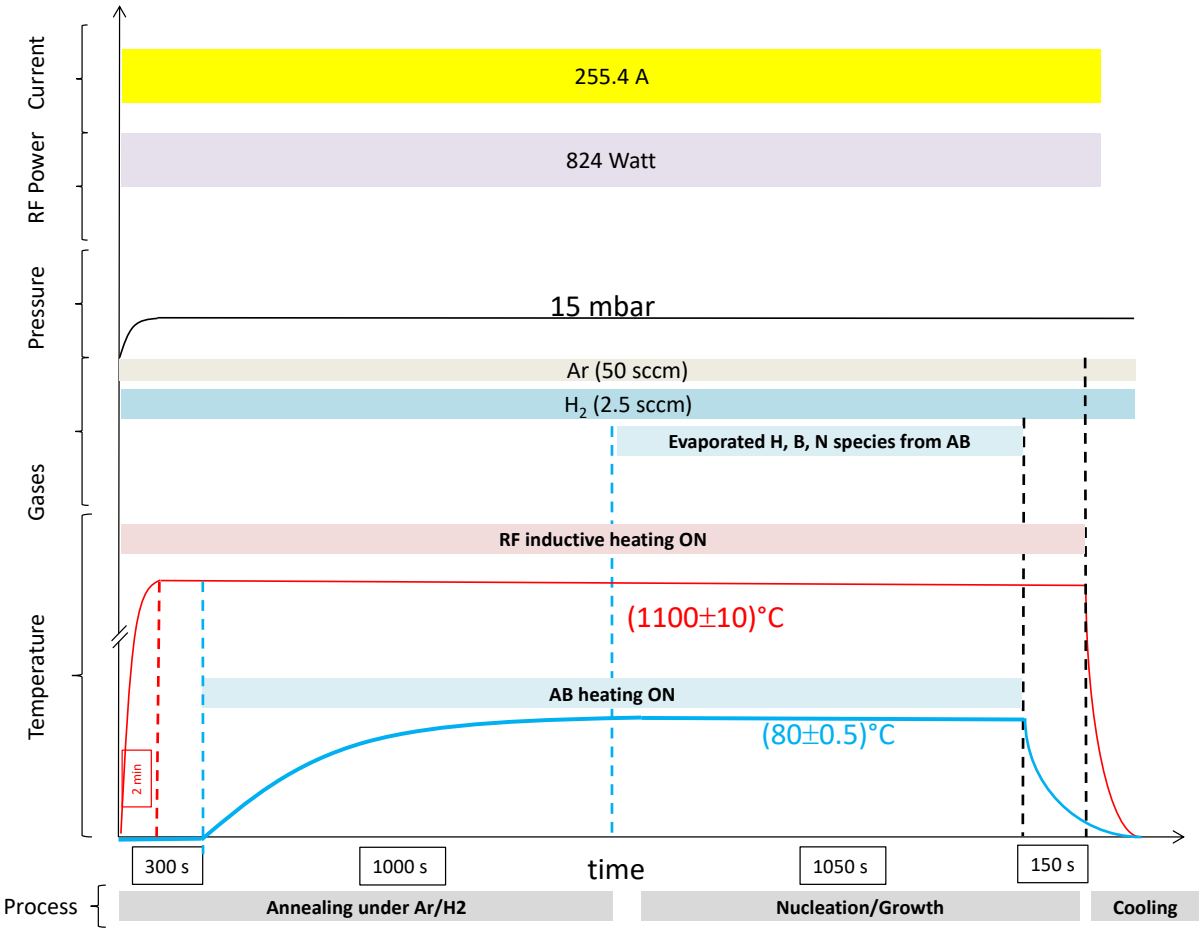


**Figure 3.** Inductive heating protocol for low pressure chemical vapor deposition of FL-BN.

Figure 3 involves the heating of AB and encompasses the following steps: (i) Initially, Cu foils were positioned atop the W foil, and the entire stack was inserted into a 1.35 cm diameter quartz tube, centrally positioned within the coils to ensure control over the temperature gradient. Simultaneously, the nickel boat containing the appropriate amount of AB was enclosed with a polymer filter, and the entire assembly was situated inside the quartz tube, with a distance of 16 cm from end to end upstream of the induction coils. (ii) The reactor was then evacuated and filled with 50 sccm of argon and 2.5 sccm of hydrogen to reach a pressure of 15 mbar. The temperature of the copper was gradually increased to 1100°C over 120 s. Subsequently, the copper temperature was maintained at 1100 °C for an additional 180 s to ensure complete melting of the Cu foil and uniform spreading on the W substrate. (iii) Following this, FL-BN growth was initiated by gradually heating the ammonia borane using the Julabo heating system until the temperature reaches 80 °C over ~1000 s. At

this temperature ammonia borane presumably starts to vaporize. (iv) Nucleation and growth of FL-BN on the liquid copper were then initiated and continued for 750 s. (v) The Julabo heating system was turned off 150 s before the heating power, followed by cooling down to room temperature under $Ar/H_2$ flow.

It is noteworthy that, based on our experiments, both the sublimation temperature and the quantity of ammonia borane have an impact on the flux of vaporized boron-nitrogen species from solid AB, consequently influencing the nucleation density, the number of layers and the size of FL-BN domains.

To transfer the as-grown FL-BN from copper to silicon wafer, electrochemical delamination known as "bubbling" method was used. First, the copper surface was coated with a supporting layer of Poly(methyl methacrylate) (950k PMMA, MicroChem) at 4500 rpm for 60 s and heated at 180°C for 1 min followed by thermal annealing at 70 °C for 2 hours. The obtained PMMA/ FL-BN/ Cu was then used as an anode in an electrochemical cell and connected to a Pt electrode acting as a cathode in (1M) aqueous NaOH solution. The voltage of 8 V applied between the catalyst foil and the Pt electrode induces the reaction $2H_2O_{(l)} + 2e^- \rightarrow H_2(g) + 2OH^-_{(aq)}$ to form hydrogen bubbles which lead to the detachment of the PMMA/ FL-BN sheet from the Cu foil. The detached PMMA/ FL-BN was then washed several times with deionized water and transferred by fishing method onto a target substrate of $SiO_2$(300 nm)/Si. Finally, the PMMA supporting layer was removed in acetone at 50°C for one hour followed by an isopropanol bath for one hour.

The analysis of FL-BN domains involved several techniques: Raman spectroscopy (HR800 from HORIBA Jobin-Yvon) was utilized in confocal mode under ambient conditions, using a 473 nm laser with a spot size of ~1 µm. This small spot size is well-suited for measuring hBN domains, allowing for acceptable spatial resolution and detailed analysis of individual features within the sample. Such resolution ensures that Raman spectroscopy can effectively characterize localized properties of the material, including variations in thickness and composition, within these domains. For scanning electron microscopy, the ZEISS MEB FEG SUPRA 40VP, equipped with high-resolution detectors, was employed to examine the samples. Additionally, the Carl Zeiss Axio Scope A1 AX10 microscope provided magnified observations with objectives of 5x, 10x, 20x, and 50x. Surface composition and chemical states were analyzed using X-ray photoelectron spectroscopy (K-Alpha+ from ThermoFischer), which featured a 1486.6 eV X-ray source, a 400 µm diameter, and 72 W

power, with general spectra acquired at 200 eV and high-resolution spectra at 40 eV. The B/N ratio in XPS can be measured by analyzing the peak areas of N1s and B1s core-level electrons, applying atomic sensitivity factors (RSF) to account for differences in emission intensities. RSFs are derived empirically from standard samples, with peak areas corrected by baseline corrections to minimize uncertainty to ±5%.

Cathodoluminescence experiments were performed at room temperature on a JEOL IT800 SEM, equipped with an AMETEK Monarc Pro system. In CL, the electron beam of the SEM creates electron-hole (e-h) pairs which give rise to spectral signatures from UV to infrared that are characteristic of the materials under investigation. This luminescence signal can reveal the presence of defects, color centers, or binded e-h, called excitons which is the relevant signal for the characterization of h-BN quality [8]. In wide band gap materials like boron nitride, excitons stay stable even at room temperature thanks to the strong Coulomb interaction between electrons and holes [40]. The BN layer thickness being limited to a few atomic layers, we took care to maximize the number of electron-hole pairs generated by choosing a low acceleration voltage of 1kV: this voltage corresponds to a mean excitation depth of 11 nm in h-BN [41]. The IT800 SEM is well adapted to work at low acceleration voltage with an ultimate spatial resolution of 0.7 nm at 1kV. We fixed the current at 1 nA thanks to the Faraday cup in the column of the SEM.

Two types of CL measurements were done: Firstly, we scanned the electron beam over the sample while recording the luminescence signal resulting in a CL image. The CL emission is filtered by an optical bandpass filter (QUANTUM DESIGN 214FS10) centered at 214 nm corresponding to the free exciton emission, the resulting signal is detected by a photomultiplier tube. Secondly, we recorded CL spectra emitted from individual triangular domains. The spectra present a spectral resolution of 0.8 nm and are corrected from the CCD and grating spectral responses.

## 2.2 Thermochemical modeling

Thermodynamic calculation of equilibrium for a specific gas mixture involves assessing the distribution of chemical species within the system at a particular temperature and pressure. In the specific case of h-BN growth, the chemical equilibrium state was estimated for an ideal gas mixture consisting of species representing the h-BN growth from ammonia borane or borazine (BZ) precursors diluted in $Ar/H_2$ mixture. Alternatively, the utilization of water

could be considered to diminish the h-BN nucleation rate. Indeed, introducing water vapor into the growth system offers an effective means to independently adjust the etching rate of h-BN, thereby allowing for modulation of h-BN nucleation density, shape, and size. This technique achieves triangular h-BN domains of up to 330 μm in size, surpassing previous results [42]. The interest of thermochemical models lies in reproducing, through computation, the chemical environment in the gas and on the substrate surface, thus enabling a better understanding of the role played by the chemical species responsible for the growth of boron nitride. Currently, 31 species have been identified to be present in the reactor including potential h-BN nucleation and growth precursors. These are: Ar, $H_2$, H, $N_2$, N, NH, $NH_2$, NNH, $N_2H_2$, $N_2H_3$, $N_2H_4$, $NH_3$, B, $B_2$, BH, $BH_2$, $BH_3$, $B_2H_6$, BN, $H_3NBH_3$ (AB), $H_2NBH_2$, $H_2BNH$, $HBNH_2$, $B(NH_2)_2$, HNBH, $BNH_2$, $H_2BN$, BNH, HBN, $B_3N_3H_6$ (BZ) and $HB(NH_2)_2$. If water is introduced into the system, it comprises a total of 62 species, including the 31 species from the H-B-N system and an additional 31 species containing oxygen. These additional species include: BO, $BO_2$, $B_2O$, $B_2O_2$, $B_2O_3$, HBO, $HBO_2$, $H_3BO_3$, $H_3B_3O_6$, HNBO, HNBOH, $B(OH)_2$, $H_2NBO$, $H_2NB(OH)_2$, $HNB(OH)_2$, $H_2NBOH$, $H_2NBHO$, $H_2NBH(OH)$ , HNBH(OH) , $HNO_3$, $HNO_2$, HNO, $H_2O$, $H_2O_2$, $HO_2$, O, $O_2$, OH, NO, $N_2O$, $NO_2$ and $NO_3$. These chemical species were identified through thermochemical calculations exploring potential combinations within the HBN system, focusing on small precursors 31 species with well-established thermodynamic data. Additionally, the HBNO system was analyzed by including 31 more species selected based on the same criteria. Collectively, these 62 species represent, to the best of our knowledge, a robust working hypothesis for assessing the thermodynamic stability of the system under specific conditions of CVD hBN growth.To find the equilibrium state representing the experimental conditions, the Ansys Chemkin x19.2 software [43] was employed. The basic theory for determining chemical equilibrium uses the principle of minimization the Gibbs free energy of a number of ns species composing the system. For a given specie k $\in$[1,ns], the standard-state Gibbs free energy $G^0_k$ was determined based on the standard-state molar enthalpy $H^0_k$ and entropy $S^0_k$. To acquire temperature-dependent values for $H^0_k$ and $S^0_k$, one could utilize either the NASA 7 or NASA 9 polynomial fits. These fits are customized to specific temperature ranges and utilize a seven-term or a nine-term functional form, respectively. While both polynomial fits are valuable for representing thermodynamic data, the NASA 9 model generally offers greater accuracy and applicability across a broader temperature spectrum, albeit with increased computational complexity. To optimize computational efficiency, we have chosen to utilize the NASA 7

format, which is compatible with Chemkin input files. A subset of these data, including $NH_3$, $BH_3$, AB, and BZ, is provided in table S1 of Supplementary materials.

Note that our thermochemical modeling is distinguished by its ability to determine the relative concentration of multiple species in the reactor, particularly concerning the elements H-B-N-O. Such a model can be implemented in a macroscale multiphysics framework as proposed by Ji *et al.* [44]. However, unlike Ji *et al.*'s approach, which focuses solely on the flow-assisted diffusion of precursors and neglects the chemical nature of species, our approach provides crucial insights into the thermodynamic stability of key species involved in h-BN growth. This can potentially lead to a more precise understanding of the growth dynamics.

## 3. Experimental results

Figure 4 depicts a scanning electron microscope image of the FL-BN sample in its as-prepared state, enhanced with color for better rendering. Numerous hierarchical FL-BN domains are observed growing on the Cu foil, confirming the reaction of the B and N precursors on the surface of the liquid metal. This observation highlights the effectiveness of inductive heating in the spontaneous growth of uniformly distributed FL-BN crystals across the entire liquid copper surface. Hexagonal boron nitride crystals exhibit a preference for growth along energetically stable edges, characterized by nitrogen (N) terminations favored over boron (B) terminations, resulting in the formation of triangular crystals. As the growth progresses, a distinct coalescence process of h-BN grains becomes evident. Randomly distributed triangular domains combine to form star-like shapes. As depicted in the image, FL-BN crystals emit with remarkably high intensity upon electron beam excitation. For instance, adlayer h-BN flakes cluster centrally on h-BN grains, denoted by the bright regions, due to the increase in boron-nitrogen thickness. Thus, liquid copper facilitates the merging of h-BN grains. Observing figure 4, it is evident that the orientations of triangular h-BN grains are not preferential, with nearly equal numbers of triangular h-BN grains in each orientation. This stands in stark contrast to h-BN grains grown on solid Cu surfaces. Indeed, previous studies have indicated that h-BN grains grown on solid Cu surfaces exhibit preferred lattice orientations with minimal stacking energy, owing to variations in stacking energy across different orientation angles.

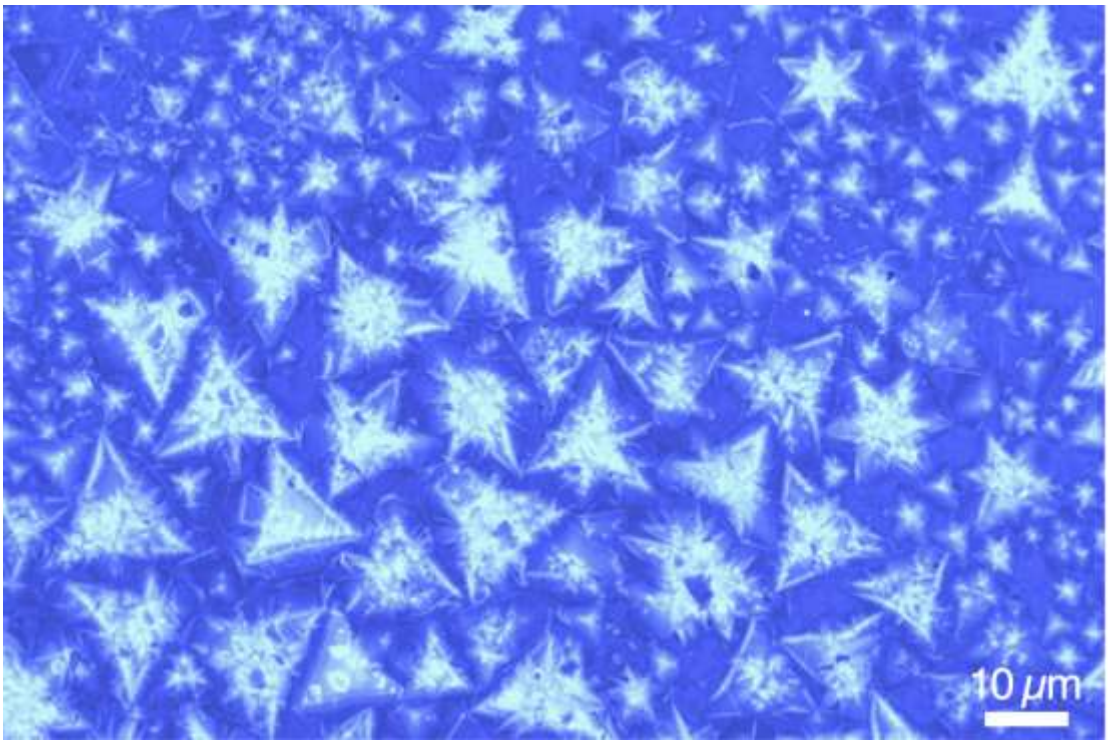


**Figure 4.** Colored SEM image of as-prepared FL-BN sample grown on liquid copper.

Conditions: Ar: 50 sccm - $H_2$: 2.5 sccm - $m_{AB}$=0.7 mg – pressure P=15 mbar – Temperatures $T_{AB}$=80°C, $T_{Cu}$=1100°C -growth time t=12.5 min (750 s).

However, when the solid Cu foil transitions into a liquid state, the Cu crystal faces vanish, leading to random orientations of h-BN grains. A magnified grayscale SEM image shown in figure 5 reveals complex hierarchical FL-BN structures with underlying atomic terraces and top-branched patterns. The as-formed FL-BN crystals begin to aggregate along six orientations, leading to the formation of several branches. These findings align with those of Geng *et al*. [21], who employed thermal CVD to grow FL-BN on liquid Cu and decomposed the hierarchical FL-BN superordered structure into two vertically stacked components: one situated beneath the FL-BN film, and the other exhibiting top-oriented branched h-BN patterns.

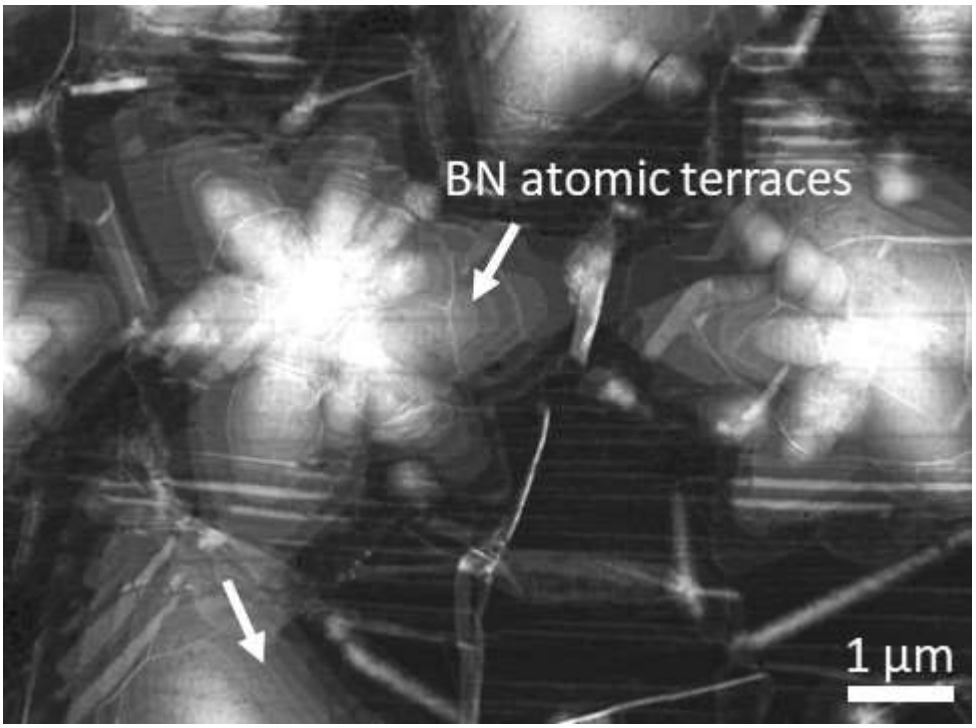


**Figure 5.** Magnified SEM images of hierarchical FL-BN structures grown on liquid copper highlighting arrowed underlying atomic terraces and top branched patterns. The as-formed FL-BN crystals start to aggregate along six orientations, and thus lead to the formation of several branches.

To confirm the material's $sp^2$-hybridized FL-BN nature, we employed Raman spectroscopy, a rapid, straightforward, and non-destructive technique. The statistical analysis of full width at half-maximum (FWHM), based on multiple Raman spectra recorded at different sample positions and illustrated in the inset of figure 6(a), reveals a range spanning from 8 $cm^{-1}$ to 24 $cm^{-1}$ corresponding to the values observed in conventional CVD methods for multilayers. While the average FWHM statistically hovers around 20 $cm^{-1}$, discrepancies in values may stem from the hierarchical nature of the FL-BN structures. Indeed, as reported in [45], FWHM tends to increase with an escalating number of h-BN layers. Thus, the lower FWHM values could arise from single atomic layer terraces, clearly discernible in the SEM image of figure 5, while higher FWHM values may be attributed to multi-layered hierarchical structures. Figure 6(b) presents a symmetrical peak positioned at 1369.3 $cm^{-1}$, while in figure 6(c), the peak is observed at 1366.0 $cm^{-1}$. The peak in figure 6(b) exhibits a FWHM of 8.8 $cm^{-1}$, whereas in figure 6(c), it widens to 19.8 $cm^{-1}$. This peak corresponds to the characteristic stretching mode (E2g) originating from the in-plane vibrations of boron and nitrogen atoms

within crystalline h-BN [45,46], further substantiating the growth of high-purity FL-BN films. Specifically, we observe the lack of additional peaks resulting from the random stacking of $sp^2$ layers, which is typical of amorphous BN (a-BN) with atomic-level structural disorder.

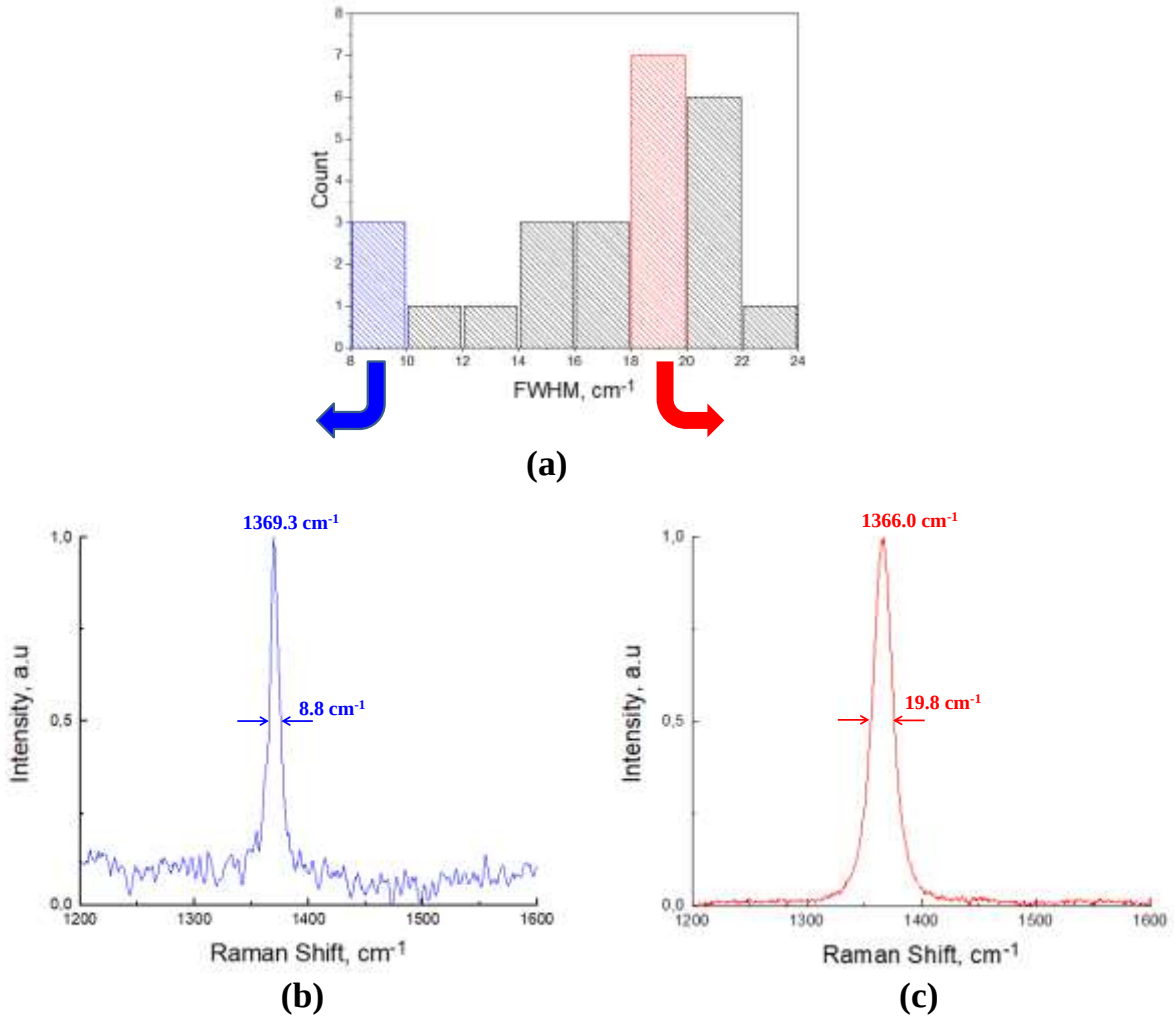


**Figure 6.** Raman spectrum of as grown FL-BN recorded at room temperature on copper substrate with laser excitation wavelength of 473 nm. (a) Statistical distribution of FWHM in $cm^{-1}$, based on multiple Raman spectra recorded at different sample positions. (b) Raman spectrum with FWHM = 8.8 $cm^{-1}$. (c) Raman spectrum with FWHM = 19.8 $cm^{-1}$.

Raman measurements in figure 6 show FWHM values of 8.8 $cm^{-1}$ and 19.8 $cm^{-1}$, indicating the presence of both single-layer h-BN and multilayer h-BN, respectively. These findings support that the atomic steps observed in the SEM images of figure 5 are primarily due to variations in the h-BN layer thickness. While substrate steps could influence the overall structure, the terraces and edges in the SEM are mostly attributed to the h-BN layers interacting differently with the electron beam.

It is important to note that the Raman spectra obtained under the same synthesis conditions but without the filter reveal poorly organized BN deposits, as shown in the Raman spectrum in figure S2 and the SEM image in figure S3 of the supplementary materials. Furthermore, the optical image in figure S4 clearly shows the disorganized BN deposits, even on the tungsten substrate, confirming the transport of nanoparticles originating from the vaporization of ammonia borane that were not captured by the filter. Calculations presented in the supplementary materials demonstrate that for nanoparticles with diameters ranging from 50 to 100 nm, the gravitational force (Fg) is significantly smaller than the drag force (Fd), indicating that these particles will be transported by the gas stream *via* advection. This behavior supports the idea that nanoparticles are carried within the reactor under our specific conditions without the filter. The SEM image in figure S3 clearly reveals the presence of predominantly spherical particles, ranging from approximately 200 nm to 1 µm. Some of these particles form a "fuzzy" hierarchical structure distributed across the copper surface, without any distinct triangular h-BN domains. This observation suggests that the nanoparticles produced during ammonia borane (AB) heating are not conducive to h-BN growth, likely due to their amorphous nature and lack of crystalline order. When these amorphous nanoparticles, along with Ar, $H_2$, and volatile $B_xN_yH_z$ species, reach the copper surface, they are more likely to grow in random, disordered directions, rather than forming well-defined, crystalline structures like the characteristic triangular h-BN domains shown in figure 4 and figure 5. This behavior aligns with the inherent disorder of amorphous materials. Consequently, in the absence of a filter, these amorphous particles tend to form irregular deposits instead of organized, crystalline domains. In contrast, the filtration system effectively prevented the amorphous nanoparticles from reaching the copper surface, allowing only volatile species to promote the nucleation and growth of well-defined h-BN domains. Figure 7(a) presents optical micrographs of a FL-BN film, obtained with a filter, and transferred onto $SiO_2$/Si. The film displays distinct optical contrast, indicating the formation of triangular forms of multilayer FL-BN with a lateral size of ~10 µm. The quality of the h-BN was further assessed using Raman spectroscopy, leveraging the sensitivity of the E2g phonon mode to the thickness and crystallinity of h-BN. In figure 7(b), the Raman spectra revealed a well-defined and intense E2g band across the surface, suggesting uniform thickness of the h-BN film. The average position of the E2g mode was determined to be 1366.3 $cm^{-1}$, closely aligned with the expected value for bulk h-BN [47] and those observed in as-grown FL-BN on copper. This consistency in frequency confirms the adequate thickness of the FL-BN film for its intended use as a substrate for other 2D materials. The narrow linewidth of the E2g band, with a full-

width at half-maximum of approximately 18.9 $cm^{-1}$, indicates the high crystallinity of the FL-BN. While slightly larger than the values reported for exfoliated flakes from h-BN single crystals (7–8 $cm^{-1}$) [8], this linewidth is significantly smaller than those observed for CVD films synthesized without a metal catalyst (25-60 $cm^{-1}$) [36,48,49] and in the same order of those of multilayer h-BN grown on catalysts with average value, 17–18 $cm^{-1}$ [50,51]. Hence, the inductive heating process demonstrates the capability to produce FL-BN films with equivalent, if not superior, crystallinity compared to the classical TCVD process, offering undeniable advantages in terms of rapidity and efficiency.

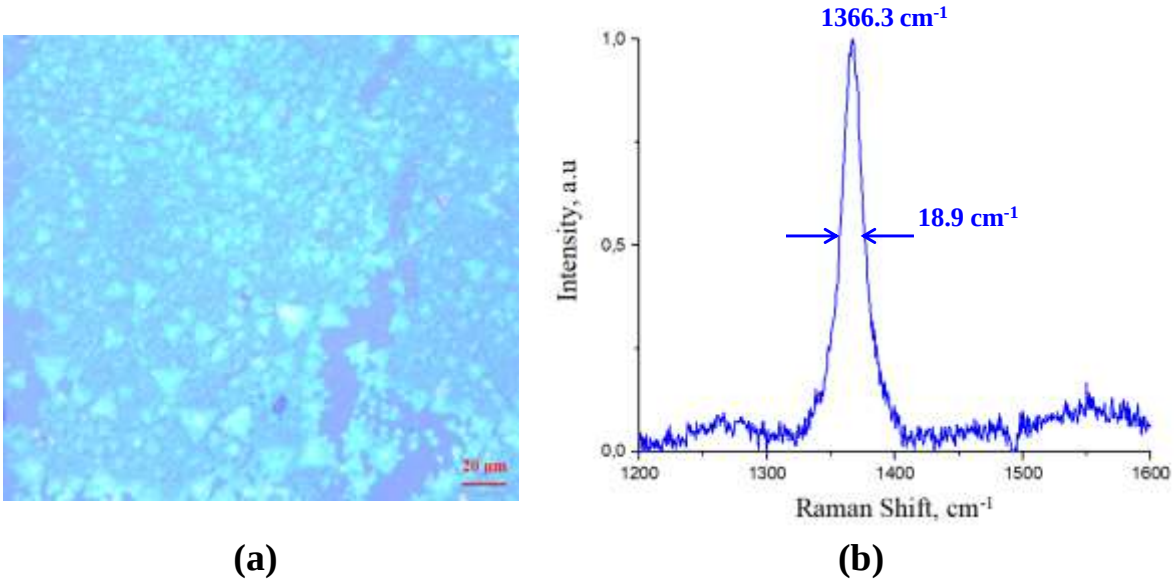


**Figure 7.** (a) Optical image of transferred FL-BN sample on $SiO_2$/Si substrate (scale bar is 20 µm); (b) Respective Raman spectrum recorded at room temperature with laser excitation wavelength of 473 nm.

To study the local chemical interactions within the FL-BN sample, we investigate the chemical bonding between boron and nitrogen atoms by analyzing the binding energy peak positions in the XPS spectrum. As shown in figure 8, XPS analysis validates the existence of two distinct single XPS peaks for N1s and B1s, detected at binding energies of 398 eV and 190.5 eV, respectively. This correspondence closely aligns with typical XPS data for $sp^2$-bonded h-BN. The atomic ratio of boron to nitrogen, estimated from the integrated peak areas in the XPS spectra, is B/N=1.18, indicating consistency with the stoichiometry of h-BN, albeit with a slight imbalance toward boron-rich material.

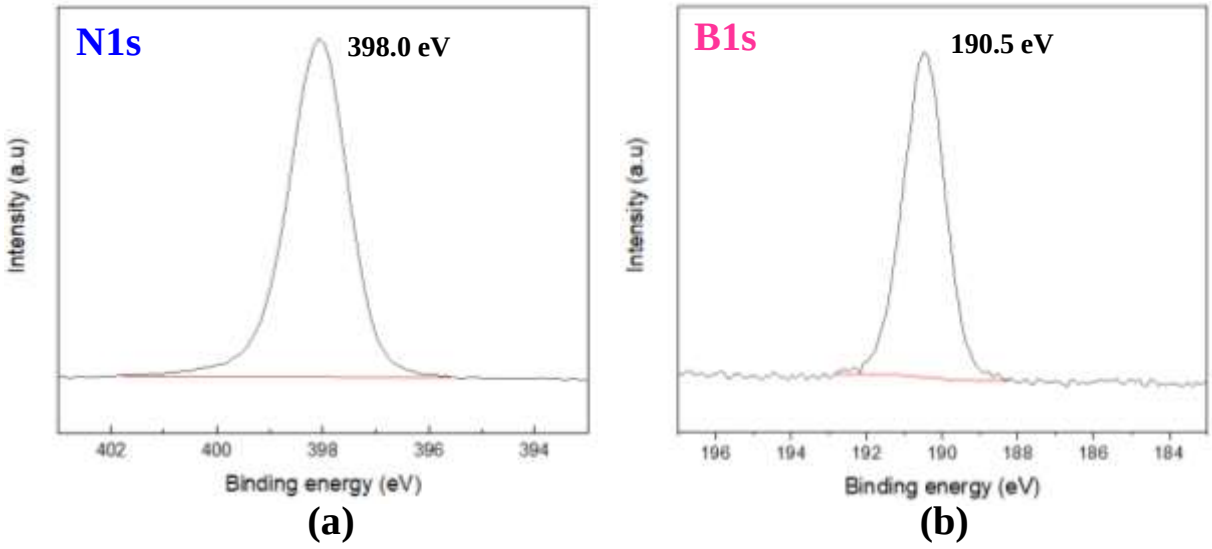


**Figure 8.** High resolution X-ray photoelectron spectroscopy XPS spectra of the FL-BN sample with associated binding energies. (a) N1s and (b) B1s.

The high quality of the BN layer is confirmed by the CL analysis revealing an intense UV emission from the triangular domains at room temperature. A CL image of the free exciton recombinations at 215 nm is presented in figure 9(b) together with the secondary electron image recorded simultaneously in figure 9(a). The thick part of the triangular domains appears the most emissive. It can be explained by the absorption of the 1 keV electron beam by the transparent BN layers, the excitation increasing with thickness. This effect might be also reinforced by a weak emission yield of BN atomic layers in luminescence experiments [8,52] compared to that of bulk crystals [40]. Low voltage excitation appears well suited to excite a few atomic layers of BN. Low voltage CL appears promising for 2D materials, for instance the UV luminescence of CVD multilayers has been scarcely observed by cathodoluminescence up to now and only at cryogenic temperature [53]. For exfoliated h-BN layers, no CL signal could be detected below 6L at 2 kV [54].

A typical CL spectrum recorded at room temperature when pointing the electron beam at the center of triangular domains of low Raman FWMH (~ 10 $cm^{-1}$) is presented in figure 10(a). It shows the exciton recombination with a maximum near 215 nm corresponding to the free exciton recombinations with the optical phonons required to overcome the indirect gap of BN multilayers. Note that the phonon lines involved in the indirect recombinations at low temperature [40] are not resolved at room temperature due to thermal broadening. A broad

band centered close to 300 nm is also observed with varying intensity among the sample, probably related to structural defects such as stacking disorder.

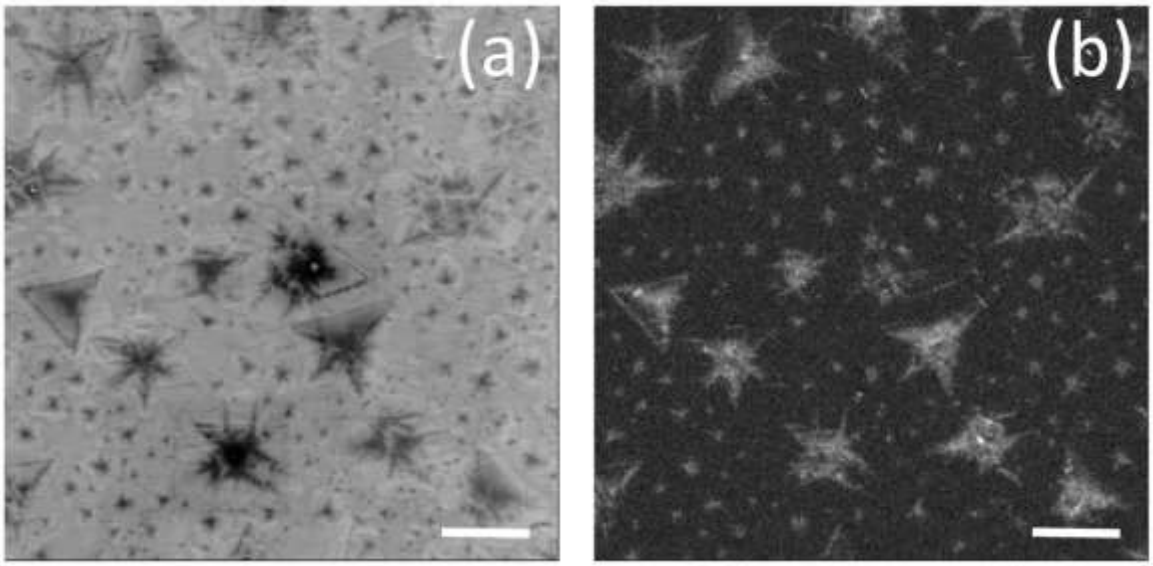


**Figure 9.** (a) SEM image (b) Room temperature CL image of the exciton luminescence filtered at 214 nm ± 5 nm. Scale bars correspond to 10 µm.

In figure 10(b), a Gaussian pic fitting was used to deconvolve four contributions at 206.6, 210.4, 214.6 and 222 nm in the deep UV spectral region. The small shoulder at 210.4 nm might indicate a different stacking than AA' in hexagonal phase, since the phonon-assisted transitions of exciton luminescence are stacking sensitive [55]. For instance the ABC stacking of the rhombohedral phase has often been reported in the CVD growth of BN multilayers [56,57] multilayers. Interestingly the 206.6 nm peak corresponds to the direct exciton (dX) in the BN multilayer, at a slightly higher energy than the indirect exciton (iX) that dominates the emission at ~215 nm [40]. Note that the direct bandgap BN monolayer emits in the same spectral range [52]. However, the accurate excitation of the thickest part of the triangular domain with a focused electron beam excludes here such a possibility. It confirms that a direct exciton emission occurs concomitantly with the indirect one in BN multilayer despite their indirect bandgap, as already pointed out in Ref. [40]. By counting the atomic terraces on high resolution images such as presented in figure 5, we estimate that the thickness of high emissive regions is of the order of 10 atomic layers. To the best of our knowledge, this is the first report of free exciton luminescence at room temperature from BN multilayers grown by CVD technique. It clearly highlights the high quality and purity of such $sp^2$ BN layers.

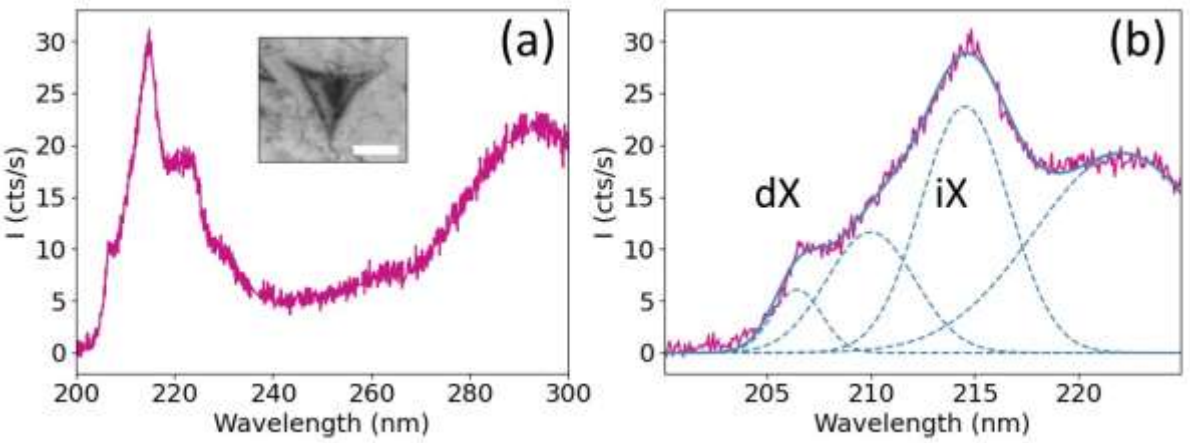


**Figure 10.** (a) Room-temperature CL spectrum of a BN multilayer taken at the center of the triangular domain shown on the SEM image in the inset (the scale bar corresponds to 5 μm). The dominant peak at ~215 nm comes from the optical recombination of free excitons in BN. (b) Deconvolution of the exciton peak with four Gaussian lines.

## 4. Results of modeling analysis

In this section, we detail the results of the simulations that align with the experimental conditions described earlier. Additionally, the model enabled us to explore the influence of several parameters, such as the flow rates of ammonia borane AB, $H_2$, and Ar, along with variations in pressure and temperature. Taking advantage of the rapidity of these calculations, we also explored the effect of the hypothetical addition of water. The thermochemical model we present is primarily intended as a design tool to explore how various parameters influence the thermodynamic stability of HBNO species, rather than to replicate the intricate details of experimental measurements. Therefore, the comparison between experimental data, such as those obtained through mass spectrometry (MS), and our model predictions should be regarded as qualitative. This comparison provides valuable insights into general trends but should not be interpreted as a precise validation of the model. It is important to note that the model incorporates assumptions and simplifications about equilibrium conditions, which are effective for capturing the key features of the decomposition process and for conducting parametric studies. However, it does not account for kinetic effects, which play a crucial role under experimental conditions, and therefore cannot provide exact quantitative predictions for species decomposition or growth dynamics.

Heating solid ammonia borane (AB) leads to sublimation, which initially increases vapor pressure and causes a rapid gas release, resulting in flow rate spikes. As sublimation progresses and particle size decreases, the flow rate may vary due to reduced surface area for mass transfer. Additionally, uneven heating and changes in gas dynamics can create fluctuations in flow rates, further complicating the process [58]. For these reasons, we chose to vary the AB flow as a parameter in the model. The ammonia borane flow rate was determined through the calibration of Chen's data [59], which experimentally explored the impact of borazine flow rate and growth duration on the number of layers of h-BN under atmospheric pressure conditions. We first replicated Chen's experimental data as depicted in figure S5 of supplementary materials. Subsequently, we examined *via* simulation how pressure and the nature of the AB and BZ precursors affect species distribution. For these calculations, AB and BZ were introduced under identical stoichiometric conditions of B and N, with an AB flow rate three times that of BZ. This ensures an equal number of B and N atoms with a slight excess of H if AB is used as a precursor. Given the low flow rates of AB and BZ considered, we can neglect this excess H effect in the calculations. The calculations

were performed at both atmospheric pressure (APCVD) and a low pressure of 15 mbar (LPCVD).

The simulation conditions are outlined in table S2 of supplementary materials, while the results are visually presented through histograms depicting species in descending order, along with the standard deviation of each species, for AB and BZ at LPCVD and APCVD, shown in figure S6 and figure S7 of supplementary materials, respectively. From this analysis, AB flow rates resulting in h-BN thicknesses ranging from 4 to 40 layers are determined to be 0.6 sccm and 1.8 sccm, respectively, as illustrated in figure S8 of supplementary materials. These values will serve as boundary conditions in our simulations of LPCVD synthesis. Since the amount of ammonia borane $m_{AB}$ as well as vaporization temperature $T_{AB}$ used experimentally was minimal, i.e. $m_{AB}$=0.7 mg and $T_{AB}$=80°C respectively, the flux of vaporized AB was set at $Q_{AB}$=0.6 sccm as a standard value to guarantee a relatively few numbers of atomic layer between 5 to 10 layers as roughly estimated from figure 5. We proceeded to adjust the key parameters of the inductive heating, adhering to both the standard values and the range of variations specified in table 1. This includes the effect of temperature and the nature of vector gas as well as the effect of the pressure, the AB and water flow rates.

**Table 1.** Parametric study during inductive heating (IH) simulations.

| | **Temperature** | **Pressure** | **Flow rates** | | | |
|---|---|---|---|---|---|---|
| **Simulation*** | **T, °C** | **P, bar** | **$Q_{Ar}$, sccm** | **$Q_{H2}$, sccm** | **$Q_{AB}$, sccm** | **$Q_{H2O}$, sccm** |
| $IH_1$ | **20-1100** | 0.015 | 50 | 2.5 | 0.6 | - |
| $IH_2$ | 1100 | **0.001-1** | 50 | 2.5 | 0.6 | - |
| $IH_3$ | 1100 | 0.015 | 50 | 2.5 | 0.6 | **0-3** |
| $IH_4$ | 1100 | 0.015 | 50 | **0-3** | **0-3** | **0-3** |

* In each row, the cells containing numbers in bold indicate the varied parameter and its range of variation.

## 4.1 Effect of growth temperature

Figure 11 illustrates the evolution of several species relative to the temperature. It demonstrates that at low temperatures, the gas is primarily composed of Ar, $H_2$, and borazine. However, as the temperature rises, $BH_2$ and $BH_3$ radicals increase in concentration at the

expense of borazine. Despite $NH_3$ showing an increase with temperature, its concentration remains relatively low. At 1100°C, figure 12 shows the molar fraction distribution of all species. In our conditions, the gas is predominantly comprised of Ar (0.943), followed by $H_2$ (0.053), $BH_2$ ($2.2\times10^{-3}$), $N_2$ ($1.1\times10^{-3}$), BZ ($1.4\times10^{-4}$), $BH_3$ ($1.0\times10^{-4}$) and $NH_3$ ($6.6\times10^{-10}$) being significantly lower. These findings suggest that borazine could act as a precursor for h-BN growth. The limited presence of $NH_3$ is attributed to the stability of $N_2$. These results support the excess of boron observed in the XPS results.

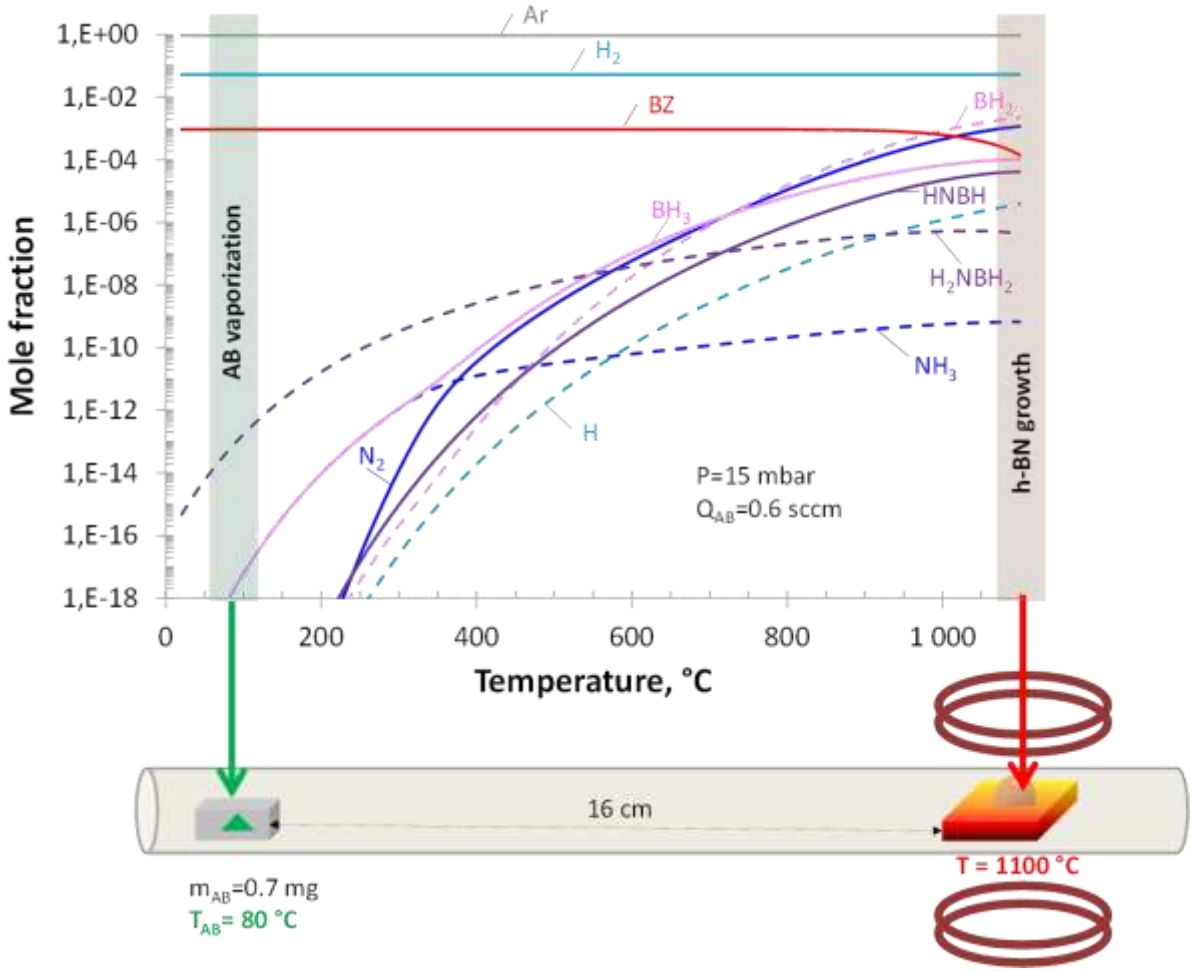


**Figure 11.** Simulated evolution of mole fraction of boron and nitrogen species as a function of temperature from AB vaporization temperature up to the zone of the copper heated by induction. Conditions: ($IH_1$ in table 1) Pressure P = 0.015 bar. Flow rates: $Q_{Ar}$=50 sccm - $Q_{H2}$=2.5 sccm - $Q_{AB}$=0.6 sccm.

Due to the near saturation of the d-orbital in copper, its ability to accommodate boron and nitrogen atoms is limited, resulting in low solubility. Consequently, the h-BN chemical vapor deposition process primarily occurs on the metal surface. The key stages of nucleation can be depicted visually, as shown in figure 13. These stages encompass critical processes such as

precursor adsorption, dehydrogenation, surface diffusion, attachment and detachment of B and N precursors at the growing edge of h-BN, and etching by atomic hydrogen. In contrast to graphene, the stability of the borazine molecule, which is already structured similarly to the unit cell of h-BN, may contribute as a parallel channel to secondary nucleation as shown in figure 13(b). This could explain the challenge in obtaining single-layer h-BN.

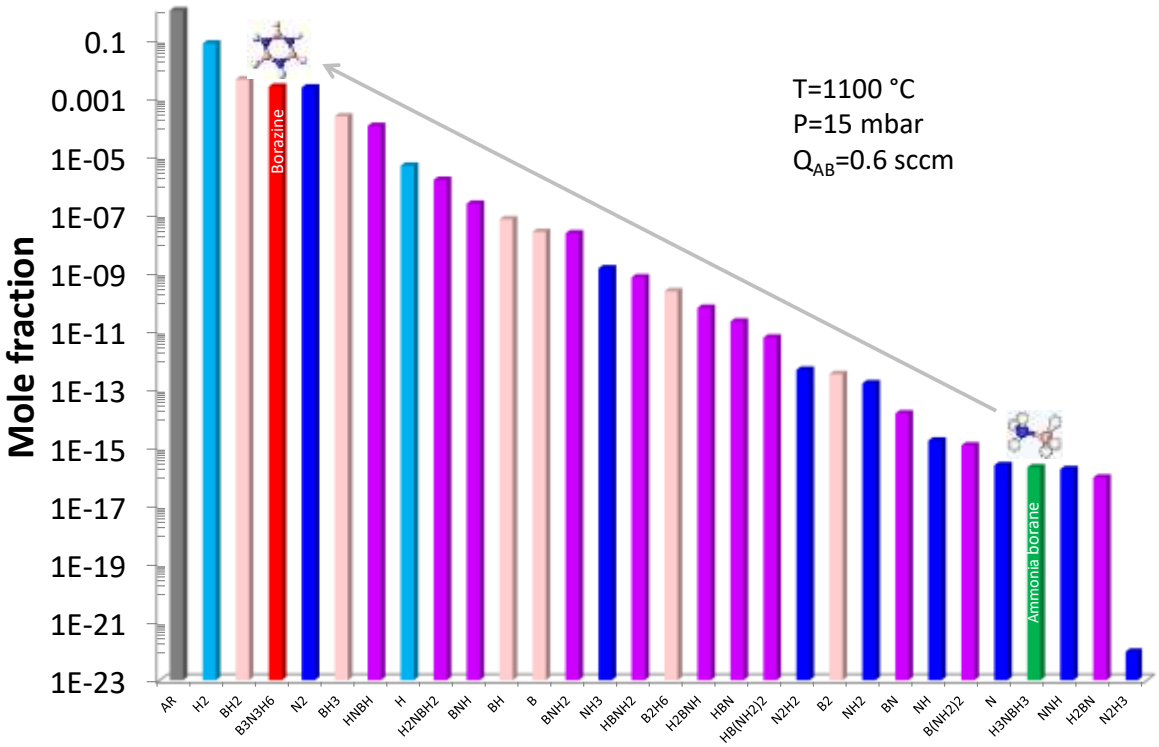


**Figure 12.** Histogram representing the distribution of all considered species in the calculation reported for a temperature of 1100°C, corresponding to liquid copper, and presented in descending order. Conditions: ($IH_1$ in table 1) Temperature = 1100°C - Pressure P = 0.015 bar. Flow rates: $Q_{Ar}$=50 sccm - $Q_{H2}$=2.5 sccm - $Q_{AB}$=0.6 sccm.

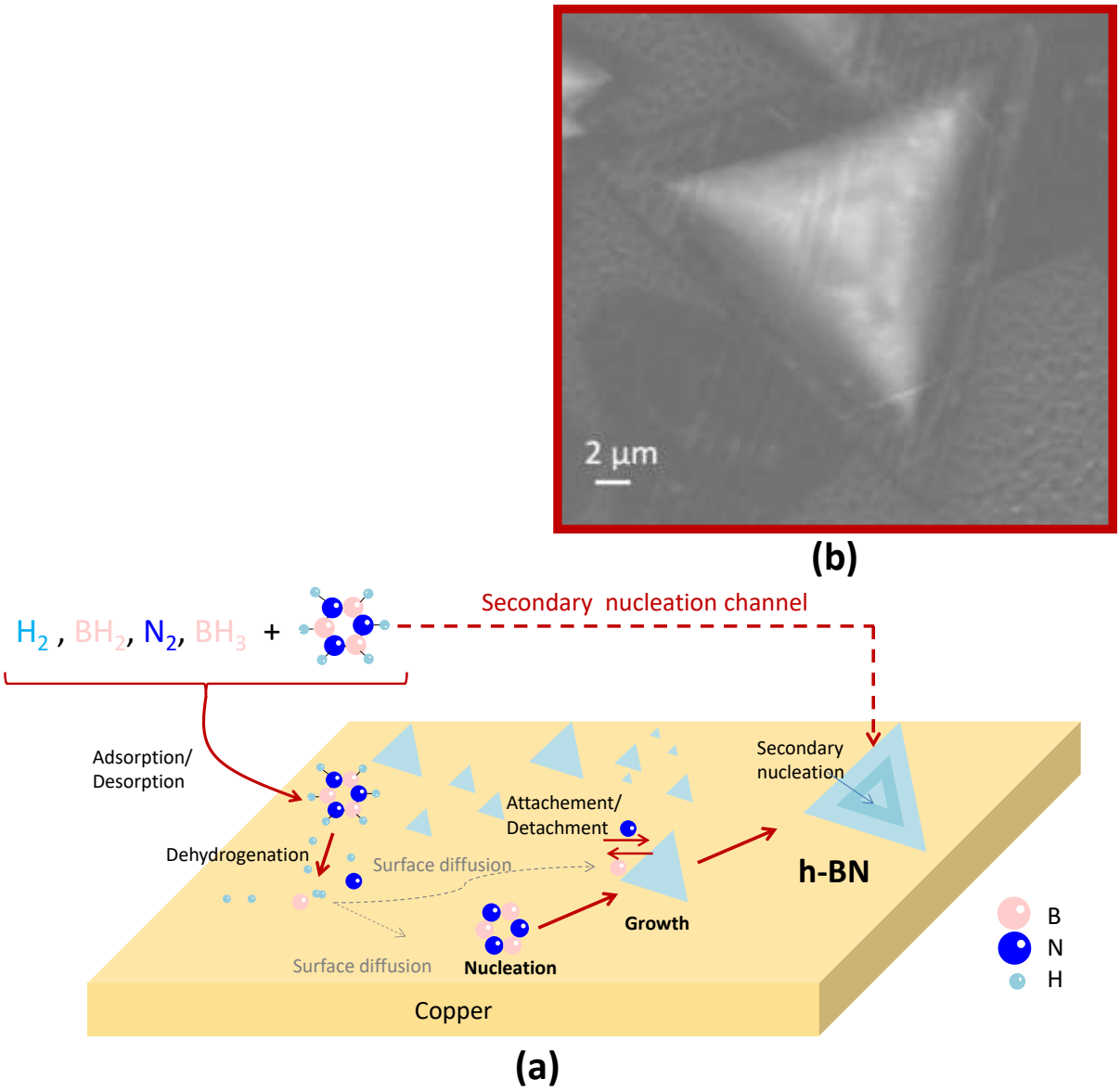


**Figure 13.** (a) Schematic representation of the h-BN CVD growth from the calculated major species. (b) SEM image of triangular FL-BN domains.

The surface reaction mechanism in figure 13(a) is based on two main findings: thermochemical calculations from this study and established literature on borazine as a growth precursor [1,60]. Our calculations (Figure 12) show that borazine, along with $BH_2$ and $BH_3$, are the dominant boro-nitrogen species generated from ammonia borane under our experimental conditions. Prior studies using borazine as a precursor, supported by *in situ* XRD and XPS, demonstrate that h-BN growth on Cu proceeds *via* borazine dissociation. This

mechanism, validated experimentally, has been adapted to ammonia borane, with borazine identified as the key intermediate. This finding suggests a similar growth mechanism when either borazine or ammonia borane is used as a precursor for h-BN growth on Cu. The main difference between the two lies in the generation of nanoparticles transported by the flux when ammonia borane is used. This issue could be mitigated by a nanofiltration step, as discussed earlier, which would allow only volatile boro-nitrogen species to pass through. This approach could lead to a universal growth mechanism, as illustrated in figure 13, for both precursors.

### 4.2 Effect of pressure

If pressure does not affect the molar fraction of $H_2$ as shown in figure 14, it appears to promote the formation of borazine at the expense of species such as $BH_2$, $BH_3$, $N_2$, HNBH, and H. However, $H_2NBH_2$ and $NH_3$ concentrations increase with pressure. An interesting observation is that at a pressure of 40 mbar under these specific calculation conditions, it divides the domain into two regions: $BH_2$ dominates if P<40 mbar, whereas borazine dominates at P>40 mbar.

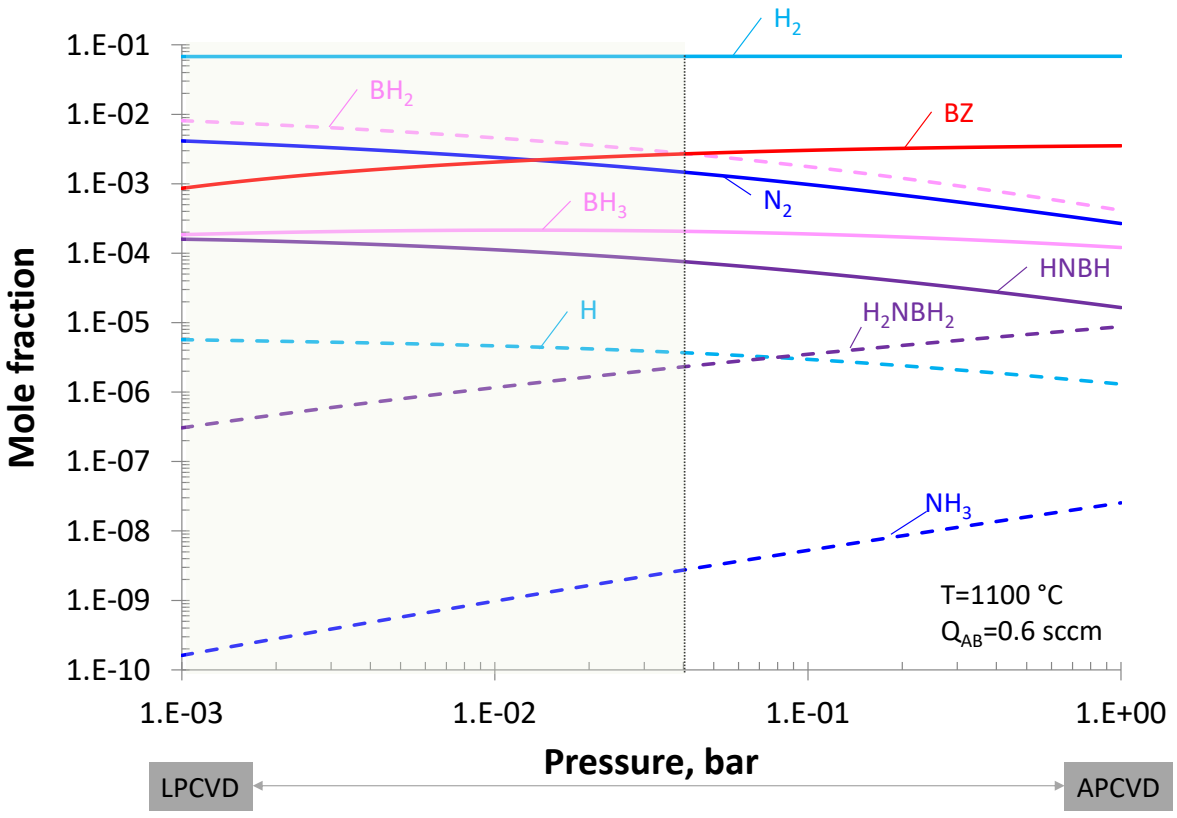


**Figure 14.** Mole fraction of major species as a function of pressure. Conditions: ($IH_2$ in table 1) Temperature T=1100°C; Flow rates: $Q_{Ar}$=50 sccm - $Q_{H2}$=2.5 sccm - $Q_{AB}$=0.6 sccm.

### 4.3 Effect of adding water

As shown by Wang *et al*. [42], the utilization of water could be considered to diminish the h-BN nucleation rate. Indeed, large-sized single crystal monolayer h-BN domains and continuous films were obtained by simply introducing a controlled amount of water vapor into the reaction zone by bubbling water with carrier gas $H_2$. As for our conditions, the ammonia borane was used as a precursor at ambient conditions and the substrate consisted of liquid Cu. This effectively tunes the etching rate of h-BN and modulates its nucleation density, shape, and size with high reproducibility. By controlling the amount of water vapor or $Ar/H_2$ flow rate ratio, the shape of h-BN domains evolves from negatively curved triangles to regular hexagons and circles, demonstrating precise kinetic growth modulation. Wang *et al*. suggest that borazine serves as the primary reactant, and they demonstrate that the addition of water vapor significantly reduces the nucleation density of h-BN grains, resulting in larger domain sizes. An excess of water vapor decreases the growth rate, causing a transformation of h-BN domain shapes from straight-edged triangles to negatively curved edges. The decrease in nucleation density is attributed to the reaction between water vapor and B atoms at high temperatures, leading to the formation of $B_2O_2$ vapor, which regulates the overall nucleation and growth of h-BN.

According to our simulations presented in figure 15, HBO and $HBO_2$ emerge as the dominant oxygen-containing species and act as nucleation regulator agents, i.e., when HBO and $HBO_2$ are present, they reduce the h-BN nucleation density. Moreover, an increase in water content drastically reduces the concentration of BZ, as depicted in figure 15.

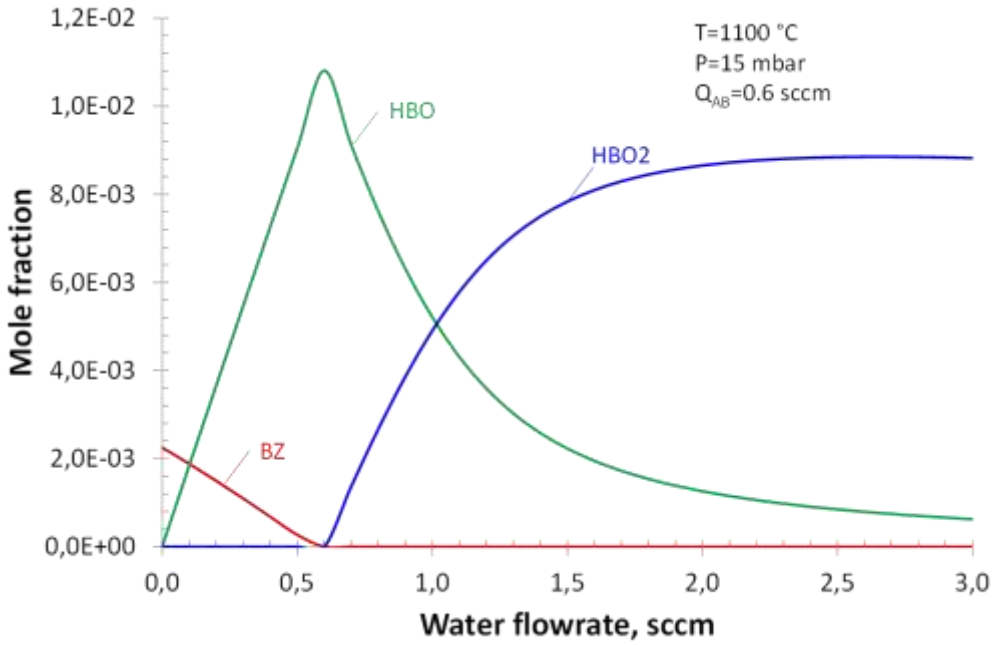


**Figure 15.** Mole fraction of the borazine and the major oxidized species as a function of water flow rate. Conditions: ($IH_3$ in table 1) Temperature T=1100°C; Pressure P = 0.015 bar; Flow rates: $Q_{Ar}$=50 sccm - $Q_{H2}$=2.5 sccm - $Q_{AB}$=0.6 sccm.

In the context of h-BN CVD growth from a borazine precursor on copper, the addition of water into the system leads to the increased formation of HBO and $HBO_2$. The increase in their mole fraction lowers the availability of the major precursor, borazine. The presence of HBO and $HBO_2$ reduces the likelihood of nucleation events, effectively slowing down the rate at which new h-BN domains form on the substrate. This slowing down of nucleation further contributes to the control over the growth process. Additionally, the reduced nucleation density means that secondary nucleation events, where borazine molecules nucleate on already formed h-BN domains, are minimized or even eliminated. As a result, the growth process tends to favor the expansion of existing h-BN domains rather than the formation of new ones. This effect could potentially lead to the formation of single-layer h-BN, as there are fewer opportunities for multiple layers to form on top of each other. Hence, the increased formation of HBO and $HBO_2$ due to the introduction of water into the system not only slows down the nucleation rate of h-BN but also promotes the growth of larger, single-layer h-BN domains by preventing secondary nucleation events.

4.4 Combined effects

The ternary diagrams depicted in figure 16 illustrate the mole fraction of borazine (BZ), HBO, and $HBO_2$ as a function of $H_2$, $H_2O$, and AB flow rates simultaneously. The calculations stem from 1330 simulations varying the 3 flow rates, each with a step of 0.3 sccm. The red-shaded area within the HBO and $HBO_2$ ternary diagrams delineates the region associated with the lowest nucleation rates. Conversely, the red-shaded region for BZ signifies the highest h-BN growth rate. The other species $BH_2$, $BH_3$, $NH_3$, and $B_2O_2$ are shown in figure S9 of supplementary materials.

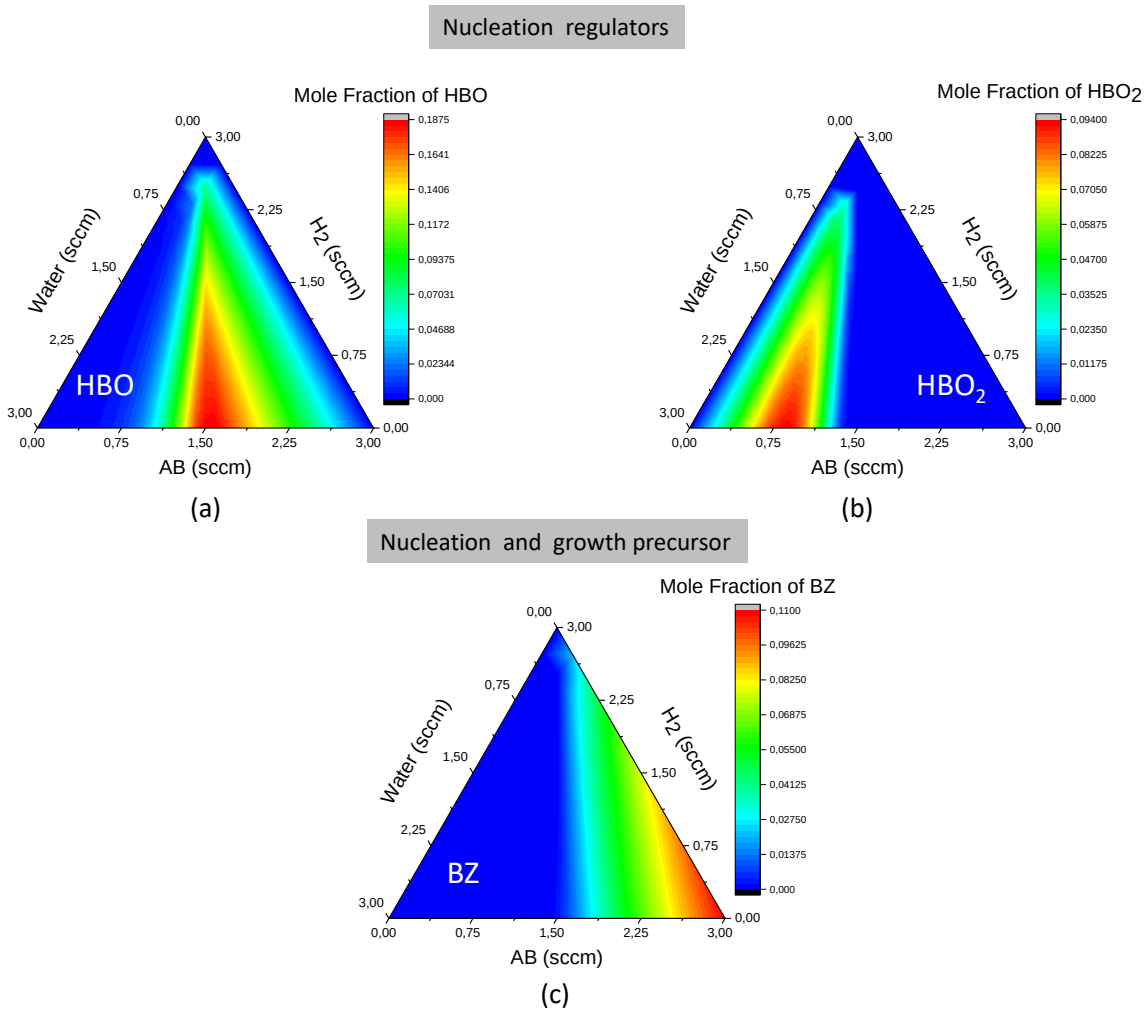


**Figure 16.** Ternary diagram showing the mole fraction of (a) HBO; (b) $HBO_2$ ; and (c) borazine (BZ) as a function of $H_2$, $H_2O$ and AB flow rates. Conditions: ($IH_4$ in table 1) Temperature T=1100°C; Pressure P = 0.015 bar; Flow rate: $Q_{Ar}$=50 sccm.

These findings suggest a trade-off between $H_2$, $H_2O$, and AB flow rates, providing a means to modulate nucleation and growth rates effectively. By adjusting the flow rates within this parameter space, one can finely tune the synthesis process to achieve desired outcomes in

terms of nucleation density and h-BN growth rate. This ultimately enables precise control over the size and morphology of h-BN domains. Based on the present study, we can propose as a perspective a new conceptual design for our inductive heating reactor. This design, illustrated in figure S10, involves a simultaneous injection of ammonia borane and water vapor into the reactor at appropriate flow rates.

## 5. Discussion

To contextualize the current discussion on hBN growth and the use of molten copper, we first highlight key advancements in this area, particularly the role of molten copper as a catalyst for 2D material growth, as well as the species determined through both experimental and modeling approaches during the ammonia borane decomposition process. The work by Geng et al. (2012) demonstrated the significant advantages of molten copper for graphene growth, providing a smooth and efficient platform for uniform film formation with minimal defects under CVD conditions [61-63]. This approach was subsequently extended to other 2D materials, including hBN, with molten copper proving highly effective for achieving high-quality, single-crystalline films. For instance, Khan et al. (2015) [20] showed that liquid copper enabled better nucleation control and the formation of higher-quality hBN films compared to solid copper. Further studies by Geng et al. (2019) [21] and Zhou et al. (2022) [22] demonstrated the ability of molten copper to facilitate the growth of lateral heterostructures and orientation-controlled hBN domains, emphasizing the potential of liquid copper for large-area, aligned 2D materials. More recent work, such as by Zhang et al. (2022) and Hao et al. (2022) [23,24], highlighted the formation of quasi-single-crystalline hBN monolayers grown on molten copper, showing the self-alignment effect driven by the liquid surface's rheological properties. While the growth of graphene and hBN on molten copper shares several advantages, the differences in material symmetry lead to distinct growth behaviors. Graphene's hexagonal structure exhibits a C6v symmetry, which governs its six-fold rotational alignment during growth, facilitating the formation of large, uniform domains with minimal grain boundaries [64]. On the other hand, hBN exhibits a trigonal C3v symmetry, resulting in a different azimuthal alignment during growth. As observed in our experiments, the random orientation of hBN flakes during growth on molten copper contrasts with the ordered alignment seen on solid copper substrates. This finding aligns with previous studies, including Geng et al. (2019), which reported that molten copper allows for the random alignment of hBN crystals, contributing to the formation of large, hierarchical

structures. In addition to symmetry differences, the solubility of precursor materials plays a crucial role in the growth dynamics of these materials. Carbon atoms from methane, used in graphene growth, exhibit relatively high solubility in molten copper, enabling efficient incorporation into the graphene lattice. In contrast, the solubility of boron and nitrogen is significantly lower in molten copper. Specifically, first-principles calculations show that carbon has the highest solubility and diffusivity in copper, while nitrogen exhibits the lowest, with boron displaying intermediate properties for both solubility and diffusivity [65]. This lower solubility of boron and nitrogen in molten copper may result in slower incorporation of these elements into the growing hBN lattice, which could explain the smaller hBN domain size of approximately 10 µm observed in our experiments, compared to the larger 100 µm domains typically seen in standard CVD graphene growth on molten copper [64]. Additionally, our study provides valuable insights into the chemical species driving hBN growth. Through modeling, we identified borazine and $BH_2$ as the dominant species resulting from ammonia borane decomposition, with secondary species such as $BH_3$. We also explored the role of water addition, which was found to reduce nucleation density and borazine concentration, thus promoting the formation of larger domains. This result is in line with the work of Jankowski et al. (2021), who observed the self-assembly of graphene flakes on molten copper, noting the impact of capillary and electrostatic forces on their alignment and coalescence. Similar principles are likely at play in our system, although the polar nature of hBN may introduce additional interfacial effects that could influence the nucleation and growth process. Moreover, our results contribute to a deeper understanding of the growth dynamics of hBN by incorporating a large number of species into our modeling framework, covering a wide range of temperature and pressure conditions. This work is consistent with recent studies, such as the one by the MIT group [66], which also sought to optimize hBN growth using machine learning to vary key parameters like substrate temperature and the flow rates of hydrogen and borazine, thereby regulating hBN domain sizes. Additionally, they identified the growth windows for achieving larger flake sizes using a Gaussian process. While the domain sizes observed in our study (around 10 µm) are slightly smaller than those reported in [66] (21.5 µm), our modeling work offers a more comprehensive understanding of the relationships between growth conditions and chemical composition, providing a clearer path for further advancements in hBN production. These findings underscore the importance of understanding the complex chemical species involved in hBN growth and the decomposition of ammonia borane, which serves as a precursor. The comparison with experimental data on ammonia borane's thermal decomposition further illuminates these

challenges. However, some discrepancies exist between the thermochemical model's predictions and experimental observations regarding gas-phase species, making this a multifaceted issue that involves both theoretical modeling and experimental validation. As part of ongoing research, it is crucial to address these contradictions comprehensively, considering the variability in experimental conditions, the intricate nature of the ammonia borane decomposition process, and the influence of factors like water contamination. The need to incorporate kinetic effects and refine thermodynamic data for intermediate species further highlights the complexity of this subject, demanding extensive analysis to reach accurate conclusions. Additionally, the ongoing development of advanced computational methods, such as ReaxFF and DFT [67-70], underscores the evolving nature of this field, making the inclusion of detailed calculations and discussions essential for advancing our understanding. The chemical species resulting from the thermal decomposition of AB have been widely debated in the literature, with research typically falling into two categories: studies exploring AB as a hydrogen source [71-77] and those investigating its role in the CVD growth of hBN. While the former has been relatively well-documented, only few studies from Babenko et al., 2017 [78], and Wood et al., 2017 [79] report *in situ* measurements by mass spectrometry of gas-phase species during hBN growth in APCVD and LPCVD, respectively. This limited number of studies is likely due to the experimental challenges and the complexities involved in interpreting such spectra in CVD hBN growth conditions. Since the pioneering studies by Shore and Parry [80] in the 1950s, ammonia borane (AB) has been recognized for its slight instability, leading to gradual hydrogen release even under ambient conditions. Extensive thermal analyses listed in Table S3 of Supplementary Information, have shown that AB decomposition is complex and heating rate-dependent, yielding both gaseous (e.g., hydrogen, borazine, aminoborane) and solid (e.g., polymeric aminoborane, $BNH_x$ polymers) products [71-77]. For CVD, ammonia borane is typically heated to temperatures between 60 and 110°C, with borazine often being identified as the active species [81-85]. A comparison of species identified through mass spectrometry analyses and those considered in our model is provided in Table S4 of the Supplementary Information. Notably, the species observed in CVD hBN growth [78,79] contradict those detected during ammonia borane thermal decomposition, likely due to variations in experimental conditions such as pressure, heating rates, gas flow rates, and reactor geometries. Specifically, the low borazine signal in mass spectra [78,79] contrasts with previous findings where borazine was a dominant product of AB decomposition [71,72,76,77], as predicted by our model. The presence of water was clearly identified in [79], as evidenced by large peaks at 17 amu (OH) and 18 amu ($H_2O$).

This water contamination could account for the very low intensity of the peak assigned to borazine in the mass spectra, suggesting that water significantly suppresses borazine formation. In this regard, figure S11a of the Supplementary Information illustrates the impact of water on the equilibrium distribution of species. In this figure, the relative abundance of species is plotted as a function of their mass (in amu). These relative abundances were calculated based on the results presented in Figure 15, encompassing all 62 species considered in the model and for selected water flow rates. The species mole fractions were normalized to $H_2$, and argon was excluded to emphasize the key chemical species. According to figure S11a, the borazine peak (81 amu) qualitatively decreases as water is introduced, indicating a suppression of borazine formation. Figure S11b further explores this trend, showing the evolution of the borazine peak as a function of the molar percentage of water in the gas feed or, equivalently, the mass percentage of water in ammonia borane. Notably, the presence of approximately 1 molar % of water in the feed gas (corresponding to approximately 28 mass % of water in ammonia borane) fully suppresses the borazine peak, rendering it undetectable in the mass spectra. In practical conditions, under typical room temperature and humidity, ammonia borane could adsorb around 10-15% by mass of water from the air. In contrast, when water vapor is carefully regulated, as demonstrated in the study by Wang et al. (2017) [42], precise control over the nucleation density and size of h-BN domains can be achieved through the intentional addition of water vapor during the growth process on liquid copper. Although these calculations assume equilibrium conditions, they offer valuable insight into the expected mass spectra based on our model's assumptions, as well as the potential for using water as an effective nucleation regulator to enhance h-BN domain size. Additionally, figure S12 shows the behavior of species transitioning from the cold upstream region to the hot region as temperature varies. However, since the model, by construction, did not account for the ammonia borane heating rate, this dynamic aspect was not considered in the analysis. As illustrated in figure S12, water promotes the formation of oxygenated species such as $H_3B_3O_6$, HBO, and $HBO_2$, thereby reducing borazine formation. This highlights the importance of careful handling and storage of ammonia borane to prevent water contamination. The interplay between water vapor and ammonia borane decomposition plays a crucial role in controlling the nucleation and growth of h-BN, with careful regulation of water vapor offering a promising strategy for tuning h-BN domain size. The insights from this study, when compared to existing research, underscore the importance of optimizing experimental conditions and refining models to fully understand the complex mechanisms involved in h-

BN growth, with a view to improving the synthesis process, controlling domain sizes, and enhancing the overall quality and scalability of CVD h-BN films for practical applications.

## 6. Conclusions

In this work, we present the proof of concept for the synthesis of FL-BN by electromagnetic induction. While this method has been proposed in the past for graphene synthesis with very promising results [86,87], to our knowledge, it has never been proposed for FL-BN synthesis until now. Our results demonstrate the possibility of producing high-quality, few-layer $sp^2$ BN domains, as evidenced by SEM images, Raman analysis, and XPS. Additionally, cathodoluminescence measurements at room temperature reveal an intense UV emission from 2D BN of about 10 atomic layers, as expected for hexagonal and rhombohedral phases having an indirect bandgap. Complementary analysis would be necessary to discriminate the stacking sequence. More generally low voltage excitation appears promising for the cathodoluminescence characterization of few-atomic-layers boron nitride. The UV luminescence observed at room temperature reveals the extremely high quality and purity of the BN multilayers that are synthesized.

We also highlight the advantages of induction as a non-contact heating method, which is fast and energetically efficient. Furthermore, our modeling study quantitatively demonstrates the predominance of specific species. Particularly, ammonia borane primarily transforms into borazine, whose relative concentration was studied under various parameters. The role of water addition has shown the potential to create oxygenated species such as HBO and $HBO_2$, which act as nucleation regulators. These findings lay the groundwork for integrating this chemical model into future computational fluid dynamics simulations of real h-BN deposition testing and production reactors, providing enhanced insights for experimental synthesis processes and reactor optimization. The model developed in this study generates extensive data on species compositions under varying conditions, providing an invaluable feature set for machine learning, as utilized in [66], to enhance predictive capabilities. Moreover, ML can drive continuous model improvement by incorporating feedback through an iterative learning process, progressively refining predictions. In light of the findings presented herein, we introduce a novel reactor design for inductive heating FL-BN synthesis, aimed at achieving better control over both single and FL-BN synthesis for various applications.

**CRediT authorship contribution statement**
Wafa Alimi: Investigation, Writing – original draft, Visualization. Christophe Arnold, Julien Barjon, Ivaylo Hinkov, Mourad S. Chérif: Methodology, Writing – review & editing. Samir Farhat: Conceptualization, Funding acquisition, Writing – review & editing, Supervision.

**Declaration of competing interest**
The authors declare no conflict of interest.

**Data availability**
Data will be made available on request.

**Acknowledgments**
ANR (Agence Nationale de la Recherche) and CGI (Commissariat à l'Investissement d'Avenir) are gratefully acknowledged for their financial support of this work through Labex SEAM (Science and Engineering for Advanced Materials and devices) ANR 11 LABX 086, ANR 11 IDEX 05 02, and ANR-14CE08-0018. This work has received funding from ESR/EquipEx + program (Grant No. ANR-21-ESRE-0031) and has been supported by Region Ile-de-France in the framework of DIM QuanTiP. We thank Christele Vilar for her help in SEM experiments and the financial support of e-diamant EQUIPEX project since the present results were obtained during the tests of the CL set-up. We thank Pr Philippe Miele from Ecole Nationale Supérieure de Chimie de Montpellier for his valuable help during project development.

## References


[1] A. E. Naclerio, P. R. Kidambi, A Review of Scalable Hexagonal Boron Nitride (h-BN) Synthesis for Present and Future Applications, Advanced Materials, **35** (6) (2023) 2207374.

[2] A. A. Balandin, S. Ghosh, W. Bao, I. Calizo, D. Teweldebrhan, F. Miao, C. N. Lau, Superior thermal conductivity of single-layer graphene, Nano Letters, **8** (3) (2008) 902–907.

[3] Q. Cai, D. Scullion, W. Gan, A. Falin, S. Zhang, K. Watanabe, T. Taniguchi, Y. Chen, E. J. G. Santos, L. H. Li, High thermal conductivity of high-quality monolayer boron nitride and its thermal expansion, Science Advanced, **5** (6) (2019) 129.

[4] G. E. Wood, A. J. Marsden, J. J. Mudd, M. Walker, M. Asensio, J. Avila, K. Chen, G. R. Gavin, N. R. Wilson, Van der Waals epitaxy of monolayer hexagonal boron nitride on copper foil: growth, crystallography and electronic band structure, 2D Materials, **2** (2) (2015) 025003.

[5] N. Guo, J. Wei, L. Fan, Y. Jia, D. Liang, H. Zhu, K. Wang, D. Wu, Controllable growth of triangular hexagonal boron nitride domains on copper foils by an improved low-pressure chemical vapor deposition method, Nanotechnology, **23** (41) (2012) 415605.

[6] Z. Liu, Y. Gong, W. Zhou, L. Ma, J. Yu, J. C. Idrobo, J. Jung, A. H. MacDonald, R. Vajtai, J. Lou P. M. Ajayan, Ultrathin high-temperature oxidation-resistant coatings of hexagonal boron nitride, Nature Communications, **4** (1) (2013) 2541.

[7] W. Wang, R. Shi, J. Wang, N. Shen, Y. Wang, H. Zhang, B. N. Chandrashekar, X. Cai, W. Zhu, A. Amini, N. Wang, C. Cheng, Free-molecular-flow modulated synthesis of hexagonal boron nitride monolayers, Crystal Growth & Design, **19** (12) (2019) 7007-7014.

[8] L. Schué, I. Stenger, F. Fossard, A. Loiseau, J. Barjon, Characterization methods dedicated to nanometer-thick hBN layers, 2D Materials, **4** (1) (2016) 015028.

[9] L. Song, L. Ci, H. Lu, P. B. Sorokin, C. Jin, J. Ni, A. G. Kvashnin, D. G. Kvashnin, J. Lou, B. I. Yakobson, P. M. Ajayan, Large scale growth and characterization of atomic hexagonal boron nitride layers, Nano letters, **10** (8) (2010) 3209-3215.

[10] Y. Shi, C. Hamsen, X. Jia, K. K. Kim, A. Reina, M. Hofmann, A. L. Hsu, K. Zhang, H. Li, Z.-Y. Juang, M. S. Dresselhaus, L.-J. Li, J. Kong, Synthesis of few-layer hexagonal boron nitride thin film by chemical vapor deposition, Nano letters, **10** (10) (2010) 4134-4139.

[11] Y. Gao, W. Ren, T. Ma, Z. Liu, Y. Zhang, W.-B. Liu, L.-P. Ma, X. Ma, H.-M. Cheng, Repeated and controlled growth of monolayer, bilayer and few-layer hexagonal boron nitride on Pt Foils, ACS Nano, **7** (6) (2013) 5199.

[12] S. M. Gilbert, T. Pham, M. Dogan, S. Oh, B. Shevitski, G. Schumm, S. Liu, P. Ercius, S. Aloni, M. L. Cohen, A. Zettl, Alternative stacking sequences in hexagonal boron nitride, 2D Materials, **6** (2) (2019) 021006.

[13] T.-A. Chen, C.-P. Chuu, C.-C. Tseng, C.-K. Wen, H.-S. Philip Wong, S. Pan, R. Li, T.-A. Chao, W.-C. Chueh, Y. Zhang, Q. Fu, B. I. Yakobson, W.-H. Chang, L.-J. Li, Wafer-scale single-crystal hexagonal boron nitride monolayers on Cu (111), Nature, **579** (7798) 2020) 219-223.

[14] W. Auwärter, T. J. Kreutz, T. Greber, J. Osterwalder, XPD and STM investigation of hexagonal boron nitride on Ni (111), Surface science, **429** (1-3) (1999) 229-236.

[15] E. Ćavar, R. Westerstrôm, A. Mikkelsen, E. Lundgren, A. S. Vinogradov, M. Ling Ng, A. B. Preobrajenski, A. A. Zakharov, N. Mârtensson, A single h-BN layer on Pt (1 1 1), Surface Science, **602** (9) (2008) 1722-1726.

[16] G. Lu, T. Wu, Q. Yuan, H. Wang, H. Wang, F. Ding, X. Xie, M. Jiang, Synthesis of large single-crystal hexagonal boron nitride grains on Cu–Ni alloy, Nature communications, **6** (1) (2015) 6160.

[17] S. Vangala, G. Siegel, T. Prusnick, M. Snure, Wafer scale BN on sapphire substrates for improved graphene transport, Scientific Report, **8** (1) (2018) 8842.

[18] S. Majety, J. Li, W. P. Zhao, B. Huang, S. H. Wei, J. Y. Lin, H. X. Jiang, Hexagonal boron nitride and 6H-SiC heterostructures, Applied Physics Letters, **102** (21) (2013).

[19] J. Li, S. Majety, R. Dahal, W. P. Zhao, J. Y. Lin, H. X. Jiang, Dielectric strength, optical absorption, and deep ultraviolet detectors of hexagonal boron nitride epilayers, Applied Physics Letters, **101** (17) (2012).

[20] M. H. Khan, Z. Huang, F. Xiao, G. Casillas, Z. Chen, P. J. Molino, H. K. Liu, Synthesis of large and few atomic layers of hexagonal boron nitride on melted copper, Scientific Reports, **5** (1) (2015) 7743.

[21] D. Geng, X. Zhao, K. Zhou, W. Fu, Z. Xu, S. J. Pennycook, L. K. Ang, H. Y. Yang, From Self-Assembly Hierarchical h-BN Patterns to Centimeter-Scale Uniform Monolayer h-BN Film, Advanced Materials Interfaces, **6** (1) (2019) 1801493.

[22] X. Zhou, X. Xue, L. Cai, S. Liu, M. Liu, G. Yu, Large-area orientation-controlled growth of hexagonal boron nitride on liquid copper, ACS Applied Electronic Materials, **4** (12) (2022) 6261-6268.

[23] Q. Zhang, H. Chen, S. Liu, Y. Yu, C. Wang, J. Han, G. Shao, Z. Yao, Self-aligned stitching growth of centimeter-scale quasi-single-crystalline hexagonal boron nitride monolayers on liquid copper, Nanoscale, 2022, **14** (8) (2022) 3112-3122.

[24] Z. Hao, X. Liu, X. Zhu, M. Zhang, M. Tang, X. Pan, Growth and characterization of uniformly distributed triangular single-crystalline hexagonal boron nitride grains on liquid copper surface, Materials Research Express, **9** (4) (2022) 045009.

[25] J. S. Lee, S. H. Choi, S. J. Yun, Y. I. Kim, S. Boandoh, J.-H. Park, B. G. Shin, H. Ko, S. H. Lee, Y.-M. Kim, Y. H. Lee, K. K. Kim, S. M. Kim, Wafer-scale single-crystal hexagonal boron nitride film via self-collimated grain formation, Science, **362** (6416) (2018) 817-821.

[26] Y.Y. Stehle, H. H. Meyer III, R. R. Unocic, M. Kidder, G. Polizos, P. G. Datskos, R. K. Jackson, S. Smirnov, I. Vlassiouk, Synthesis of hexagonal boron nitride monolayer: control of nucleation and crystal morphology, Chemistry of Materials, **27** (23) (2015) 8041-8047.

[27] L. Wang, B. Wu, L. Jiang, J. Chen, Y. Li, W. Guo, P. Hu, Y. Liu, Growth and etching of monolayer hexagonal boron nitride, Advanced Materials, **27** (33) (2015) 4858-4864.

[28] S. Sharma, K. Sharma, M. S. Rosmi, Y. Yaakob, M. I. Araby, H. Ohtani, G. Kalita, M. Tanemura, Morphology-controlled synthesis of hexagonal boron nitride crystals by chemical vapor deposition, Crystal Growth & Design, **16** (11) (2016) 6440-6445.

[29] J. Yin, J. Yu, X. Li, J. Li, J. Zhou, Z. Zhang, W. Guo, Large single-crystal hexagonal boron nitride monolayer domains with controlled morphology and straight merging boundaries, Small, **11** (35) (2015) 4497-4502.

[30] R. Y. Tay, H. J. Park, G. H. Ryu, D. Tan, S. H. Tsang, H. Li, W. Liu, E. H. Tong Teo, Z. Lee, Y. Lifshitz, R. S. Ruoff, Synthesis of aligned symmetrical multifaceted monolayer hexagonal boron nitride single crystals on resolidified copper, Nanoscale, **8** (4) (2016) 2434–2444.

[31] J. C. Koepke, J. D. Wood, Y. Chen, S. W. Schmucker, X. Liu, N. N. Chang, L. Nienhaus, J. W. Do, E. A. Carrion, J. Hewaparakrama, A. Rangarajan, I. Datye, R. Mehta, R. T. Haasch, M. Gruebele,

G. S. Girolami, E. Pop, J. W. Lyding, Role of pressure in the growth of hexagonal boron nitride thin films from ammonia- borane, Chemistry of Materials, **28** (12) (2016) 4169–4179.

[32] B. Poelsema, A. Acun, L. Schouten, F. Derkink, M. Tsvetanova, Z. Zhang, H. J. W. Zandvliet, A. v. Houselt, Polar edges and their consequences for the structure and shape of hBN islands, 2D Materials, **6** (3) (2010) 035010.

[33] Y. Gao, W. Ren, T. Ma, Z. Liu, Y. Zhang, W.-B. Liu, L.-P. Ma, X. Ma, H.-M. Cheng, Repeated and controlled growth of monolayer, bilayer and few-layer hexagonal boron nitride on Pt foils, ACS Nano, **7** (6) (2013) 5199–5206.

[34] Y. Uchida, S. Nakandakari, K. Kawahara, S. Yamasaki, M. Mitsuhara, H. Ago, Controlled growth of large-area uniform multilayer hexagonal boron nitride as an effective 2D substrate, ACS Nano, **12** (6) (2018) 6236–6244.

[35] P. Thevenin, A. Soltani, A. Bath, Synthesis of hexagonal boron nitride thin films by a plasma assisted chemical vapor deposition method, Journal de Physique IV, **11** (PR3) (2001) Pr3-803-Pr3-810.

[36] H. Park, T. K. Kim, S. W. Cho, H. S. Jang, S. I. Lee, S.-Y. Choi, Large-scale synthesis of uniform hexagonal boron nitride films by plasma-enhanced atomic layer deposition, Scientific reports, **7** (1) (2017) 40091.

[37] M. Yamamoto, H. Murata, N. Miyata, H. Takashima, M. Nagao, H. Mimura, Y. Neo, K. Murakami, Low-temperature direct synthesis of multilayered h-BN without catalysts by inductively coupled plasma-enhanced chemical vapor deposition, ACS OMEGA, **8** (6) (2023) 5497-5505.

[38] K. Pashova, E. Dhaouadi, I. Hinkov, O. Brinza, Y. Roussigné, M. Abderrabba, S. Farhat, Graphene synthesis by inductively heated copper foils: reactor design and operation, Coatings, **10** (4) (2020) 305.

[39] E. Dhaouadi, W. Alimi, M. Konstantakopoulou, I. Hinkov, M. Abderrabba, S. Farhat, Graphene synthesis by electromagnetic induction heating of oxygen-rich copper foils, Diamond and Related Materials, **132** (2023) 09659.

[40] L. Schué, L. Sponza, A. Plaud, H. Bensalah, K. Watanabe, T. Taniguchi, F. Ducastelle, A. Loiseau, A. Betz, J. Barjon, Bright Luminescence from Indirect and Strongly Bound Excitons in h-BN, Physical review letters, **122** (6) (2019) 067401.

[41] S. Roux, C. Arnold, E. Carré, E. Janzen, J. H. Edgar, C. Maestre, B. Toury, C. Journet, V. Garnier, P. Steyer, T. Taniguchi, K. Watanabe, A. Loiseau, J. Barjon, Surface recombination and out-of-plane diffusivity of free excitons in hexagonal boron nitride, Physical Review B, **109** (15) (2024) 155305.

[42] L. Wang, B. Wu, H. Liu, L. Huang, Y. Li, W. Guo, X. Chen, P. Peng, L. Fu, Y. Yang, P. Hu, Y. Liu, Water-assisted growth of large-sized single crystal hexagonal boron nitride grains, Materials Chemistry Frontiers, **1** (9) (2017) 1836-1840.

[43] R. J. Kee, F. M. Rupley, J. A. Miller, M. E. Coltrin, J. F. Grcar, E. Meeks, H. K. Moffat, A. E. Lutz, G. Dixon-Lewis, M. D. Smooke, J. Warnatz, G. H. Evans, R. S. Larson, R. E. Mitchell, L. R. Petzold, W. C. Reynolds, M. Caracotsios, W. E. Stewart, P. Glarborg, C. Wang, O. Adigun, CHEMKIN Collection, Release 3.6, Reaction Design, Inc., San Diego, CA. 2000.

[44] Y. Ji, K. Momeni, L.-Q. Chen, A multiscale insight into the growth of h-BN: effect of the

Enclosure, 2D Materials, **8** (3) (2021) 035033.

[45] R. V. Gorbachev, I. Riaz, R. R. Nair, R. Jalil, L. Britnell, B. D. Belle, E. W. Hill, K. S. Novoselov, K. Watanabe, T. Taniguchi, A. K. Geim, P. Blake, Hunting for Monolayer Boron Nitride: Optical and Raman Signatures, arXiv preprint arXiv:1008.2868, (2010).

[46] R. Geick, C. H. Perry, G. Rupprecht, Normal modes in hexagonal boron nitride, Physical Review **146** (2) (1966) 543.

[47] Q. Cai, D. Scullion, A. Falin, K. Watanabe, T. Taniguchi, Y. Chen, E. J. G. Santos, L. H. Li, Raman Signature and Phonon Dispersion of atomically thin boron nitride, Nanoscale, **9** (9) (2017) 3059-3067.

[48] A.-R. Jang, S. Hong, C. Hyun, S. I. Yoon, G. Kim, H. Y. Jeong, T. J. Shin, S. O. Park, K. Wong, S. Kyu Kwak, N. Park, K. Yu, E. Choi, A. Mishchenko, F. Withers, K. S. Novoselov, H. Lim, H. Suk Shin, Wafer-Scale and Wrinkle-Free Epitaxial Growth of Single-Orientated Multilayer Hexagonal Boron Nitride on Sapphire, Nano letters, **16** (5) (2016) 3360-3366.

[49] J. Lee, A. V. Ravichandran, J. Mohan, L. Cheng, A. T. Lucero, H. Zhu, Z. Che, M. Catalano, M. J. Kim, R. M. Wallace, A. Venugopal, W. Choi, L. Colomb, J. Kim, Atomic Layer Deposition of Layered Boron Nitride for Large-Area 2D Electronics, ACS applied materials & interfaces, **12** (32) (2020) 36688-36694.

[50] Y. Uchida, S. Nakandakari, K. Kawahara, S. Yamasaki, M. Mitsuhara, H. Ago, Controlled Growth of Large-Area Uniform Multilayer Hexagonal Boron Nitride as an Effective 2D Substrate, ACS Nano, **12** (6) (2018) 6236-6244.

[51] Y. Uchida, K. Kawahara, S. Fukamachi, H. Ago, Chemical Vapor Deposition Growth of Uniform Multilayer Hexagonal Boron Nitride Driven by Structural Transformation of Metal Thin, ACS Applied Electronic Materials, **2** (10) (2020) 3270-3278.

[52] A. Rousseau, L. Ren, A. Durand, P. Valvin, B. Gil, K. Watanabe, T. Taniguchi, B. Urbaszek, X. Marie, C. Robert, G. Cassabois, Monolayer Boron Nitride : Hyperspectral Imaging in the Deep Ultraviolet, Nano Letters, **21** (23) (2021) 10133-10138.

[53] S. M. Kim, A. Hsu, M. H. Park, S. H. Chae, S. J. Yun, J. S. Lee, D.-H. Cho, W. Fang, C. Lee, T. Palacios, M. Dresselhaus, K. K. Kim, Y. H. Lee, J. Kong, Synthesis of large-area multilayer hexagonal boron nitride for high material performance, Nature communications, **6** (1) (2015) 8662.

[54] L. Schué, B. Berini, B. Plaçais, F. Ducastelle, J. Barjon, A. Loiseau, A. Betz, Dimensionality effects on the luminescence properties of hBN, Nanoscale, **8** (13) (2016) 6986-6993.

[55] M. Zanfrognini, A. Plaud, I. Stenger, F. Fossard, L. Sponza, L. Schué, F. Paleari, E. Molinari, D. Varsano, L. Wirtz, F. Ducastelle, A. Loiseau, J. Bargon, Distinguishing diffrent stackings in layered materials via luminescence spectroscopy, Physical Review Letters, **131** (20) (2023) 206902.

[56] H. Prevost, A. Andrieux-Ledier, N. Dorval, F. Fossard, J. S. Mérot, L. Schué, A. Plaud, E. Héripré, J. Barjon, A. Loiseau, Heteroepitaxial growth of sp2-hybridized boron nitride multilayer on nickel substrates by CVD: the key role of the substrate orientation, 2D Materials, **7** (4) (2020) 045018.

[57] J. Hadid, I. Colambo, J. Avila, A. Plaud, C. Boyaval, D. Deresmes, N. Nuns, P. Dudin, A. Loiseau, J. Barjon, X. Wallart, D. Vignaud, Molecular beam epitaxial growth of multilayer 2D-boron nitride on Ni substrates from borazine and plasma-activated nitrogen, Nanotechnology, **34** (3) (2022) 035601.

[58] F. Maury, F.-D. Duminica, F. Senocq, Optimization of the vaporization of liquid and solid CVD precursors: Experimental and modeling approaches, Chemical Vapor Deposition, **13** (11) (2007) 638-643.

[59] X. Chen, Chemical Vapor Deposition of Hexagonal Boron Nitride Multilayers. Department of Physics PhD thesis Technical University of Denmark, (2020).

[60] P. R. Kidambi, R. Blume, J. Kling, J. B. Wagner, C. Baehtz, R. S. Weatherup, R. Schloeg, B. C. Bayer, S. Hofmann, In Situ Observations during Chemical Vapor Deposition of Hexagonal Boron Nitride on Polycrystalline Copper, Chemistry of Materials, **26** (22) (2014) 6380-6392.

[61] D. Geng, B. Wu, Y. Guo, L. Huang, Y. Xue, J. Chen, G. Yu, L. Jiang, W. Hu, Y. Liu, Uniform Hexagonal Graphene Flakes and Films Grown on Liquid Copper Surface, Proc. Natl. Acad. Sci, **109** (21) (2012) 7992−7996.

[62] D. Kuten, K. Dybowski, R. Atraszkiewicz, Piotr Kula, Quasi-monocrystalline graphene crystallization on liquid copper matrix, Materials, **13** (11) (2020) 2606.

[63] D. Geng, G. Yu, Liquid catalysts: an innovative solution to 2D materials in CVD processes, Materials Horizons, **5** (6) (2018) 1021-1034.

[64] M. Jankowski, M. Saedi, F. La Porta, A. A. Manikas, C. Tsakonas, J. S. Cingolani, M. Andersen, M. de Voogd, G. J. C. van Baarle, K. Reuter, C. Galiotis, G. Renaud, O. V. Konovalov, I. M. N. Groot, Real-time multiscale monitoring and tailoring of graphene growth on liquid copper, Acs Nano, **15** (6) (2021) 9638-9648.

[65] X. Hu, T. Björkman, H. Lipsanen, L. Sun, A. V. Krasheninnikov, Solubility of boron, carbon, and nitrogen in transition metals: getting insight into trends from first-principles calculations, The Journal of Physical Chemistry Letters, **6** (16) (2015) 3263-3268.

[66] J.-H. Park, A.-Y. Lu, M. M. Tavakoli, N. Y. Kim, M.-H. Chiu, H. Liu, T. Zhang, Z. Wang, J. Wang, L. G. P. Martins, Z. Luo, M. Chi, J. Miao, J. Kong, Revealing Variable Dependences in Hexagonal Boron Nitride Synthesis via Machine Learning, Nano Letters, **23** (11) (2023) 4741-4748.

[67] N. Nayir, Q. Mao, T. Wang, M. Kowalik, Y. Zhang, M. Wang, S. Dwiveti, G.-U. Jeong, Y. K. Shin, A. van Duin, Modeling and simulations for 2D materials: a ReaxFF perspective, 2D Mater, **10** (3) (2023) 032002.

[68] S. S. Han, J. K. Kang, H. M. Lee, A. C. T. van Duin, W. A. Goddard, The theoretical study on interaction of hydrogen with single-walled boron nitride nanotubes. I. The reactive force field ReaxFFHBN development, J. Chem. Phys, **123** (11) (2005) 114703.

[69] M. R. Weismiller, A. C. T. van Duin, J. Lee, R. A. Yetter, ReaxFF reactive force field development and applications for molecular dynamics simulations of ammonia borane dehydrogenation and combustion, J. Phys. Chem. A, **114** (17) (2010) 5485–5492.

[70] A. Lele, P. Krstic, A. C. T. van Duin, ReaxFF force field development for gas-phase hBN nanostructure synthesis, J. Phys. Chem. A, **126** (4) (2022) 568–582.

[71] M. G. Hu, R. A. Geanangel, W. W. Wendlandt, Thermal decomposition of ammonia borane: Thermogravimetric, differential thermal, and thermo-manometric studies, Thermochimica Acta, **23** (2) (1978) 249-255.

[72] G. Wolf, J. Baumann, F. Baitalow, F. P. Hoffmann, Thermal decomposition of ammonia borane: Thermogravimetric, differential scanning calorimetric, and volumetric analysis studies, Thermochimica Acta, **343** (1-2) (2000) 19-25.

[73] F. Baitalow, J. Baumann, G. Wolf, K. Jaenicke-Rößler, G. Leitner, Thermal decomposition of ammonia borane: Kinetic studies and analysis of the gaseous decomposition products, Thermochimica Acta, **391** (2002) 159.

[74] J. Baumann, E. Baitalow, G. Wolf, Thermal decomposition of ammonia borane: Isothermal TGA/DSC measurements and investigation of the decomposition products, Thermochimica Acta, **430** (1-2) (2005) 9-14.

[75] M. Bowden, T. Kemmitt, W. Shaw, N. J. Hess, J. Linehan, M. Gutowski, B. Schmid, T. Autrey, Decomposition of ammonia borane: In situ NMR study and insight into the mechanism of hydrogen release, Mater. Res. Soc. Symp. Proc., **927** (2006) 9-14.

[76] S. Frueh, R. Kellett, C. Mallery, T. Molter, W. S. Willis, C. King'ondu, S. L. Suib, Thermal decomposition of ammonia borane: Reaction pathways and implications for hydrogen storage, Inorganic Chemistry, **50** (3) (2011) 783-792.

[77] A. C. Stowe, W. J. Shaw, J. C. Linehan, B. Schmid, T. Autrey, The thermal decomposition of ammonia borane and its reaction mechanisms, Physical Chemistry Chemical Physics, **9** (15) (2007) 1831-1836.

[78] V. Babenko, G. Lane, A. A. Koos, A. T. Murdock, K. So, J. Britton, S. Shayan Meysami, J. Moffat, N. Grobert, Time dependent decomposition of ammonia borane for the controlled production of 2D hexagonal boron nitride, Scientific Reports, **7** (1) (2017) 14297.

[79] G. E. Wood et al., In situ gas analysis during the growth of hexagonal boron nitride from ammonia borane, Mater. Res. Express, **4** (2017) 115905.

[80] S. G. Shore; R. W. Parry, The crystalline compound ammonia-borane,[1] $H_3NBH_3$, Journal of the American Chemical Society, **77** (22) (1955) 6084-6085.

[81] K. H. Lee, H. J. Shin, J. Lee, I. Y. Lee, G. H. Kim, J. Y. Choi, S. W. Kim, Large-Scale Synthesis of High-Quality Hexagonal Boron Nitride Nanosheets for Large-Area Graphene Electronics, Nano Letters, **12** (2) (2012) 714–718.

[82] R. Y. Tay, M. H. Griep, G. Mallick, S. H. Tsang, R. S. Singh, T. Tumlin, E. H. T. Teo, S. P. Karna, Growth of large single-crystalline two-dimensional boron nitride hexagons on electropolished copper, Nano Letters, **14** (2) (2014) 839–846.

[83] R. Y. Tay, X. Wang, S. H. Tsang, G. C. Loh, R. S. Singh, H. Li, G. Mallick, E. H. Tong Teo, A systematic study of the atmospheric pressure growth of large-area hexagonal crystalline boron nitride film, Journal of Materials Chemistry C, **2** (9) (2014) 1650.

[84] J. Han, J. Y. Lee, H. Kwon, J. S. Yeo, Synthesis of wafer-scale hexagonal boron nitride monolayers free of aminoborane nanoparticles by chemical vapor deposition, Nanotechnology, **25** (14) (2014) 145604.

[85] X. Song, Q. Li, J. Ji, Z. Yan, Y. Gu, C. Huo, Y. Zou, C. Zhi, H. Zeng, A comprehensive investigation on CVD growth thermokinetics of h-BN white graphene, 2D Materials, **3** (3) (2016) 035007.

[86] R. Piner, H. Li, X. Kong, L. Tao, I. N. Kholmanov, H. Ji, W. H. Lee, J. W. Suk, J. Ye, Y. Hao, S. Chen, C. W. Magnuson, A. F. Ismach, D. Akinwande, R. S. Ruoff, Graphene synthesis via magnetic inductive heating of copper substrates, ACS Nano, **7** (9) (2013) 7495–7499.

[87] E. Dhaouadi, W. Alimi, I. Hinkov, M. Abderrabba, S. Farhat, Graphene synthesis by electromagnetic induction heating: Domain size and morphology control, Diamond and Related Materials, **144** (2024) 111009.